Active Transport in Chaotic Rayleigh-Bénard Convection

Christopher Omid Mehrvarzi

Thesis submitted to the Faculty of the
Virginia Polytechnic Institute and State University
in partial fulfillment of the requirements for the degree of

Master of Science
in
Mechanical Engineering

Mark Paul, Chair
Bahareh Behkam
Danesh Tafti

December 5, 2013
Blacksburg, Virginia

Keywords: Transport, Rayleigh-Bénard convection, Spatiotemporal chaos

Active Transport in Chaotic Rayleigh-Bénard Convection

Christopher Omid Mehrvarzi

(ABSTRACT)

The transport of a species in complex flow fields is an important phenomenon related to many areas in science and engineering. There has been significant progress theoretically and experimentally in understanding active transport in steady, periodic flows such as a chain of vortices but many open questions remain for transport in complex and chaotic flows. This thesis investigates the active transport in a three-dimensional, time-dependent flow field characterized by a spatiotemporally chaotic state of Rayleigh-Bénard convection. A nonlinear Fischer-Kolmogorov-Petrovskii-Piskunov reaction is selected to study the transport within these flows. A highly efficient, parallel spectral element approach is employed to solve the Boussinesq and the reaction-advection-diffusion equations in a spatially-extended cylindrical domain with experimentally relevant boundary conditions. The transport is quantified using statistics of spreading and in terms of active transport characteristics like front speed and geometry and are compared with those results for transport in steady flows found in the literature. The results of the simulations indicate an anomalous diffusion process with a power law $2 \leq \gamma \leq 5/2$ – a result that deviates from other superdiffusive processes in simpler flows, and reveals that the presence of spiral defect chaos induces strongly anomalous transport. Additionally, transport was found to most likely occur in a direction perpendicular to a convection roll in the flow field. The presence of the spiral defect chaos state of the fluid convection is found to enhance the front perimeter by $t^{3/2}$ and by a perimeter enhancement ratio $r_p = 2.3$.

This work was supported by NSF grant award number: 0747727

Acknowledgments

I would like to thank my advisor, Professor Mark Paul, for granting me the opportunity to work in his group and for all of his insights, assistance, and encouragement throughout my graduate work. To quantify the value of his contributions would be vain and perhaps better left for an investigation into the nature of quality itself. I would also like to thank Professor Bahareh Behkam and Professor Danesh Tafti for serving as my committee members and taking the time to review and critique my work. More generally, I am grateful for *all* of the teachers and mentors I've worked with in the past five and a half years at Virginia Tech at both the graduate and undergraduate level. Their inspirational teaching have challenged me to rise above mediocrity and address difficult problems with confidence. I would like to extend a special acknowledgement to my brilliant labmates, both past and present: Dr. Alireza Karimi, Brian Robbins, Mu Xu, and Stephen Epstein - thanks for all of your help and fellowship. Finally, I would like to thank my beloved parents, Jeanne and Shahram, for their unconditional love and support throughout my studies. Without them, I would not have been able to do anything.

Contents

List of Figures

List of Tables

Chapter 1

Introduction

1.1 Motivation

The transport of a scalar species is an important phenomenon related to many areas of scientific and engineering interest. Species transport in a bulk fluid motion which does not affect the motion of the fluid is defined as passive transport. Examples of passive transport include dye diffusing within a liquid, advecting particles in the Earth's atmosphere and oceans, and the mixing of non-reacting chemicals. Active transport is defined by an additional consideration of a source, or reaction term to the transport equation – this additional term may also be coupled to the fluid velocity field to add complexity to the transport model. Examples of active transport include the combustion of premixed gases, transport of biological organisms in the oceans, and chemical oscillators, like the extensively studied Belousov-Zhabotinski reaction which has been quantified to yield chaotic dynamics even in the presence of simple stirred flows [36]. Within the scope of this thesis, the investigation of active transport is limited to the presence of a reaction and a traveling front that does *not* affect the surrounding fluid flow.

The transport of a passive species in a flow field is described by the advection-diffusion (AD) equation. These systems have been studied both numerically and experimentally for a range of flow regimes – from time-independent to turbulent flow. There has been significant progress understanding transport in steady periodic flows such as a ring of vortices. The transport of a passive species in these simplified time-independent flows can be described as an overall normal diffusive process which can be modeled by an effective diffusion coefficient due to the presence of a flow field. The presence of time-independent flows have been shown theoretically [31] and experimentally [38] to enhance the transport of a passive scalar where the effective diffusion coefficient scales proportionally with the square-root of the fluid velocity, $v^{1/2}$. Transport is also enhanced in time-dependent flows. Experiments done with time-dependent cellular flow show transport enhanced $1-3$ orders of magnitude

higher than that that of time-independent flows [37]. Furthermore, it has been shown that transport in this flow regime is independent of the molecular diffusion of the tracer used – a conclusion that further reinforces the importance of the flow field characteristics on the species transport. The results of these past experiments have shed light on a well-defined transition from slow, diffusion-limited transport in time-independent flows to fast advective-dominated transport in turbulent flows.

Likewise, active transport has an extensive literature. Much work has been done with transport described by reaction-diffusion (RD) systems due to their complex dynamics and pattern-forming qualities [8]. These systems have been used to model such biological phenomenon as action potential dynamics in neurons [15], heart dynamics [5], and chemical morphogenesis [41]. However, life is not static; many biological systems experience transport due to a bulk fluid motion. An example of this can be seen in the motion of plankton blooms in the Earth's oceans. The motion of these species in the oceans is important for the regulation of carbon and other chemicals in the atmosphere and are significant in regulating global temperatures [12]. The transport of an active scalar species within a flow field is described by the reaction-advection-diffusion (RAD) equation. Typically in RAD systems the fluid advection is significant to the motion and shape of the reaction front. A well-known theory described by Fisher and Kolmogorov [19] predicts front propagation speed as a function of molecular diffusion coefficient and reaction kinetics; however, this front speed changes with advection and a more detailed theory has yet to be developed.

There have been many studies to develop this theory, especially for active transport in simple laminar flow regimes. Active transport with reaction laws described by the Fischer-Kolmogorov-Petrovskii-Piskunov (FKPP) and Arrhenius type were explored in numerical simulations to show enhancement for front prorogation due to the presence of simple flows [1]. In systems with open-streamline flows, the front velocity, v_f was found to be proportional to the typical fluid velocity, U. In cellular flows, the front velocity is enhanced by a factor $U^{1/4}$ and $U^{3/4}$ depending on whether the advection is relatively fast or slow [2]. It has been shown that the presence of these flow fields enhance the reaction due to fluid motion distorting the reaction fronts and thereby increasing the surface area for the reaction kinetics to occur. However, critical values of fluid advection in cellular flows do exist which can also lead to reaction front extinction [42]. Similar front motion inhibition in addition to other interesting dynamics have been seen in experiments with propagating reaction fronts of an excitable Belousov-Zhabotinski (BZ) reaction. Experiments with the BZ reaction in a driven oscillatory chain of vortices identified a mode-locking phenomenon of the reaction front as a function of the amplitude and frequency of the flow field oscillation [29]. This mode-locking phenomenon is common in many systems in nature, an example of which include circadian rhythms [14]. Furthermore, experiments showed the chemical oscillations of the BZ reaction synchronized with the flow field oscillations when the transport in the flow became superdiffusive [28]. Transport inhibition of the reaction front was seen in this oscillating chain flow

when an overall wind was imposed. In these flows, the freezing of the propagation fronts was a function of the range of imposed winds and the strength of the vorticity of the flow field. This front freezing, or pinning, has also been found in cellular flows [33].

Another novel method that is being pursued to describe active transport in advecting flows is through the use of burning invariant manifolds (BIMs). These manifolds are the active transport analogy to Lagrangian coherent structures (LCS) for passive transport. LCS, known by some as the "hidden skeleton of fluid flows", are more rigorously described as the most local repelling or attracting strainlines in a flow field [30]. These stainlines have been used to effectively identify barriers in a flow field that prohibit transport of advected material. BIMs can be derived theoretically by modeling a propagating front by a system of ordinary differential equations [22]. Experiments have shown that these propagating fronts of the BZ reaction converge to these theoretical calculated BIMs for time-independent and periodically driven flows [25]. Furthermore, experimental evidence suggest that these BIMs collapse onto LCS in the limit of advection-dominated transport [4].

Indeed we can see from the wealth of research that has been done on RAD and AD systems that advection has a significant impact on the transport of a species. One open question that remains is whether the results that have been discussed so far are recoverable in systems where the convecting fluid is complex, *i.e.*, flow fields that exhibit spatiotemporal chaos. It is known already that chaotic transport can occur in simple time-dependent flow fields. Aref's [3] numerical investigations of simple mixing procedures of a passive tracer in a two-point vortex flow suggests the existence of chaotic mixing. Numerical simulations of spatially-extended fluid convection domains [7] showed passive transport enhancement due to the presence of more complex, spiral defect chaos flow field that scaled with laws similar to those found in experiments of cellular rolls in Rayeligh-Bénard convection [37]. The existence of the two transport scaling regimes is described by the effect of local wavenumber orientation. For large advection-dominated transport, the diffusivity of the passive species is enhanced locally in the direction orthogonal to the local wavevector but suppressed in the direction of the local wavevector [7].

The idea of transport enhancement in these complex flows is an attractive idea for engineering applications at the micro- and nano-scale where transport enhancement which cannot be done by inducing turbulence due to the small characteristic length scales. One such example is "lab-on-a-chip" micro-fluidic devices [17]. One question that remains unaddressed is how a reaction front behaves in the presence of a spatially-extended, complex flow field. This thesis will address this question by studying direct numerical simulations of the transport of an active scalar species in a three-dimensional, time-dependent flow field given by the chaotic state of Rayleigh-Bénard convection. The active transport that is studied is a unidirectional, "burn-type" reaction where a species transforms from states $A \rightarrow B$. This thesis will shed light on this fundamental example of transport in spatially-extended systems.

1.2 Thesis outline

In the preceding section, some current research related to active transport in various flow conditions was presented to motivate the reader to the topic. Chapter 2 of this thesis will discuss theoretical details about two different flow fields: a ring of vortices and Rayleigh-Bénard convection. The equations governing each of the flow phenomenon and their non-dimensional parameters will be discussed to highlight important physical insights. Additionally, the equations governing the transport of a species will be introduced followed by a presentation of the important time scales relevant to the transport of an active species in Rayleigh-Bénard convection. Chapter 2 will conclude with a discussion of the computational fluid dynamics solver, Nek5000, and the numerical technique used to solve the full partial differential equations. Chapter 3 will present the results of the simulations proposed in the preceding chapter. The techniques used to quantify the transport will be defined followed by a discussion of the analysis. Chapter 4 will conclude this thesis with suggestions on future research paths forward.

Chapter 2

Problem description and numerical procedure

2.1 Introduction

In this chapter, two flow fields central to this thesis investigation of transport will be discussed: a time-independent ring of vortices, and a time-dependent, chaotic state of Rayleigh-Bénard convection. By doing so, we will reinforce the evidence that time-independent convection rolls have on the transport of a species, and then investigate how the spatiotemporal chaos of these convection roll patterns further affects these transport characteristics. The equations describing these phenomena and important parameters that arise from nondimensionalization will be explored. The computational domains for each of the flow fields will be presented with their respective, experimentally relevant boundary conditions. A discussion of the numerical procedure to solve the partial differential equations will conclude this chapter.

2.2 Ring of vortices

A time-independent chain of vortices is a simple laminar flow that has many real-world applications such as mixing in industrial processes. As reviewed in the previous chapter, transport of both active and passive species within this type of flow field have been well documented. A common function used to model these type of flow fields in a rectangular domain is

$$\psi(x,y) = \frac{U\lambda}{2\pi}\sin\left(\frac{2\pi x}{\lambda}\right)\sin\left(\frac{2\pi y}{\lambda}\right) \tag{2.1}$$

where $\psi(x, y)$ is the stream function of the x-direction and y-direction velocity fields $u(x, y)$ and $v(x, y)$, λ represents a wavelength, and U is the characteristic velocity of the flow field. The aspect ratio for this rectangular domain is defined as

$$\Gamma = \frac{y}{x}. \tag{2.2}$$

The corresponding contour plot of the stream function in Eq. (2.1) with a wavelength $\lambda = 2$ and a characteristic fluid velocity $U = 1$ for $\Gamma = 10$ is presented in Fig. 2.1 as an example.

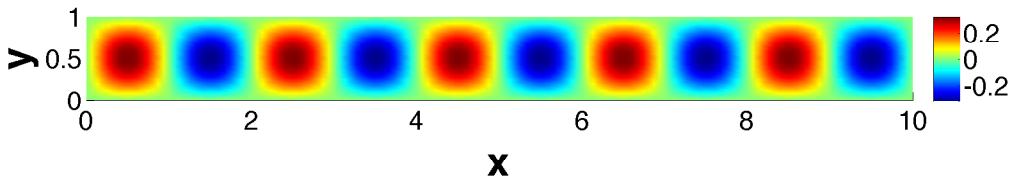

Figure 2.1: The stream function $\psi(x, y)$ for a two-dimensional, time-independent ring of vortices for a domain with an aspect ratio $\Gamma = 10$. The colors indicate the magnitude of the stream function and the directionality of the rotation.

The progression of a nonlinear reaction within this type of flow field is shown in Fig. 2.2 for times (a) $t = 0$ (b) $t = 0.2$ and (c) $t = 0.4$. The reaction highlights the behavior of these "burn-off" type reactions where a mixture of reactants which in the figure is represented in blue undergoes a reaction and transforms into products which are represented in red. Previous studies of active transport in these time-independent flow fields show front speed enhanced by a factor of $U^{1/4}$ in a "fast" advecting regime and enhanced by a factor of $U^{3/4}$ in a "slow" advecting regime [1] [2]. Simple explicit numerical simulations of transport within the flow field depicted in Fig. 2.1 show a similar transport enhancement regime as can be seen in the results in Fig. 2.3. Both the results shown in Fig. 2.3 and within the literature suggests that the presence and strength of the convection rolls have and affect on the reaction front speed. This thesis will investigate this mode of enhancement further by the addition of varied roll orientation within a large spatially-extended domain due to chaotic flow patterns.

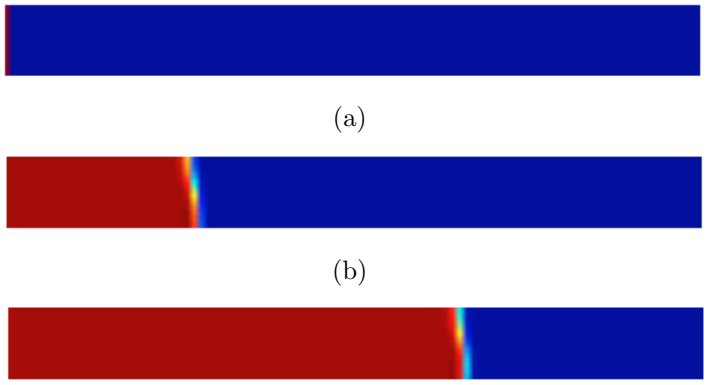

Figure 2.2: The evolution of a reaction in a two-dimensional, time-independent ring of vortices for $\Gamma = 10$ at times (a) $t = 0$, (b) $t = 0.2$, and (c) $t = 0.4$. Red represents the products and blue represents the reactants.

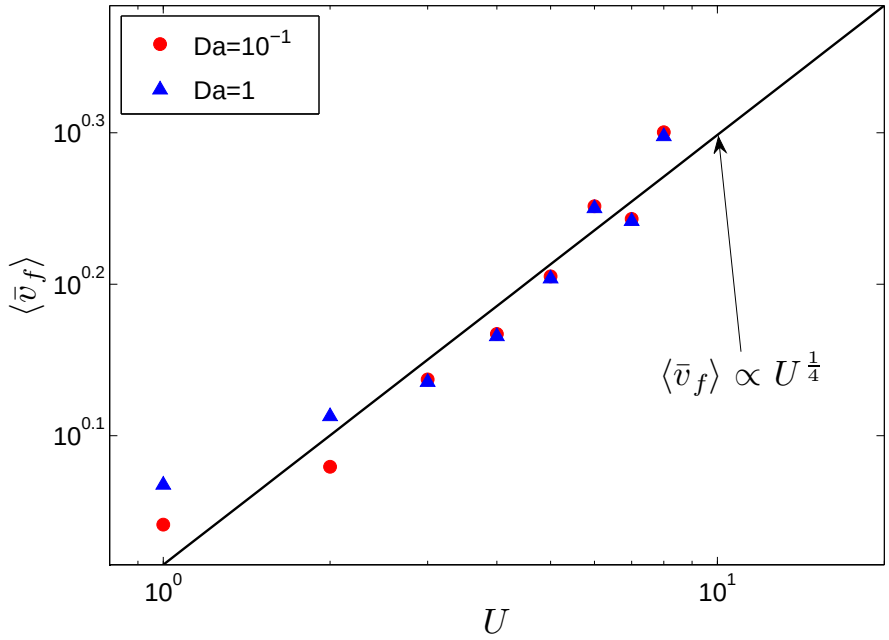

Figure 2.3: Transport enhancement in a two-dimensional ring of vortices. Here the average speed of the reaction front $\langle \bar{v}_f \rangle$ is plotted as a function of the characteristic fluid velocity U for Damköhler numbers $Da = 10^{-1}$ and $Da = 1$ on a log-log plot. The black line indicates a curve fit with a slope equal to 1/4. This power law behavior is similar to those found in [2] for advection-dominated reactions.

2.3 Rayleigh-Bénard convection

Rayleigh-Bénard convection is the natural convection that occurs when a horizontal layer of fluid is heated from below and cooled from the top normal to the direction of the gravitational force. This results in a temperature gradient across the domain that causes a change in density in a quiescent fluid and results in a buoyancy force exerted in the direction of gravity. This buoyancy force is matched by the viscous forces in the fluid in the opposing direction which prevents fluid motion. The ratio between the buoyancy and viscous forces can be quantified by the Rayleigh number,

$$\mathcal{R} = \frac{\alpha g d^3}{\nu \kappa} \Delta T \tag{2.3}$$

where β is the coefficient of thermal expansion, g is the gravitational constant, ν is the kinematic viscosity, α is the thermal diffusivity, and ΔT is the temperature difference, $T_h - T_c$. In this form, the Rayleigh number can be seen as a non-dimensional measure of the temperature difference across the domain – the Rayleigh number increases as the temperature difference ΔT increases. When ΔT reaches a critical value, the buoyancy force overcomes the viscous force which causes fluid motion to begin. The critical Rayleigh number, $\mathcal{R}_c$, is defined as the Rayleigh number at which this convective instability occurs. The quantity used to describe the Rayleigh number relative to the critical Rayleigh number is the reduced Rayleigh number which is defined as

$$\epsilon = \frac{\mathcal{R} - \mathcal{R}_c}{\mathcal{R}_c}. \tag{2.4}$$

Rayleigh-Bénard convection is the canonical form for studying nonlinear and complex phenomenon such as the weather due to its experimental accessibility. Large spatially-extended cylindrical domains, like the one shown in Fig. 2.4 are important to these types of studies and will be the domain investigated in this thesis. The critical Rayleigh number for this domain was determined experimentally to be $\mathcal{R}_c \approx 1708$ [8]. At a Rayleigh number of $\mathcal{R}_c$, time-independent convection rolls develop across the domain. When the temperature difference is increased further the convection rolls undergo another instability and become time-dependent. In this phase, the convection rolls begin forming intricate patterns, merging and annihilating with each other to form complex patterns of spirals and defects. When the temperature difference is increased further, the convection rolls break down into a cascade of smaller eddies until the flow becomes fully turbulent.

The aspect ratio for the convection domain shown in Fig. 2.4 is defined as the ratio of the cylinder's radius to the depth,

$$\Gamma = \frac{r_0}{d} \tag{2.5}$$

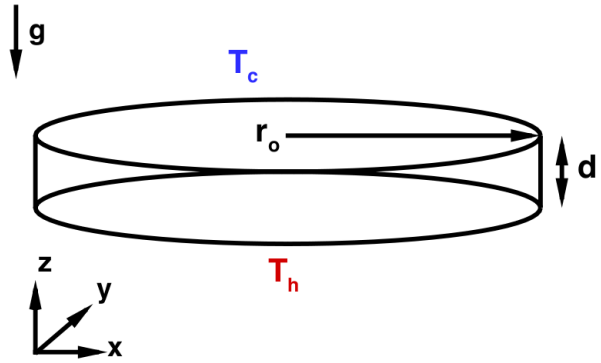

Figure 2.4: Schematic of a spatially-extended cylindrical Rayleigh-Bénard convection cell. The top wall is held at a cold temperature T_c and the bottom wall a hot temperature T_h. The width of the domain is d and r_0 is the radius. The direction of the gravitational field is indicated by g.

where r_0 is the radius and d is the depth of the domain. For the spatially-extended systems that are of interest in this thesis, aspect ratios of $\Gamma \geq 10$ are investigated. Typical temperature fields to the pattern-forming range of Rayleigh-Bénard convection are shown in Fig. 3.1(e) for the $\Gamma = 10$ domain and in Fig. 3.2(c) for the $\Gamma = 40$ domain.

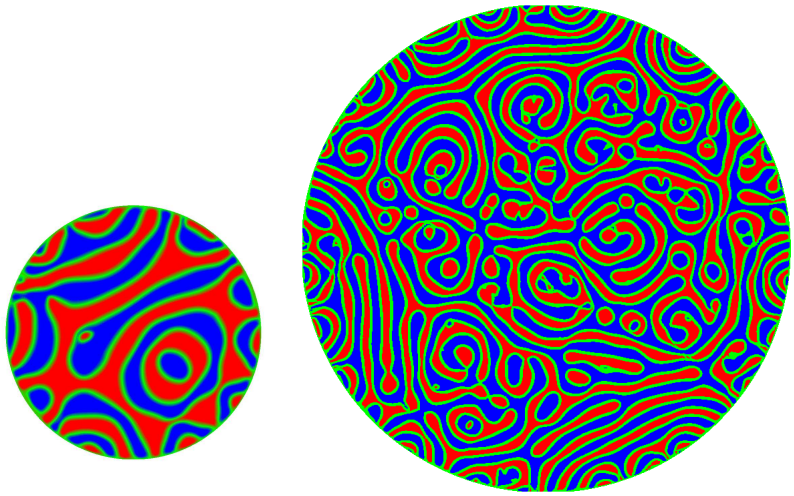

(a) (b)

Figure 2.5: Typical flow fields visualized by midplane temperature values for the (a) $\Gamma = 10$ and (b) $\Gamma = 40$ domains. The red color represents hot rising fluid while the blue color represents cold sinking fluid. Both of these flow fields exhibit spatiotemporally chaotic dynamics at a Rayleigh number of $\mathcal{R} = 6000$ ($\epsilon = 2.51$).

2.3.1 Governing equations

The partial differential equations that govern the fluid flow are the Navier-Stokes equations where the body force is represented with a buoyancy term that is a function of the density gradient in the fluid. In Rayleigh-Bénard convection, this density gradient is assumed to be a function of only temperature – a common assumption which is known as the Boussinesq approximation. The Boussinesq approximation is mathematically described as

$$(\rho_\infty - \rho) \approx \rho\beta\,(T - T_\infty). \tag{2.6}$$

where ρ_∞ and T_∞ are the reference density and temperature, respectively, and β is the volumetric thermal expansion coefficient which measures the change in density due to temperature while the pressure is held constant. The resulting momentum, mass and energy equations once the Boussinesq approximation is applied are

$$\sigma^{-1}(\partial_t + \vec{u}\bullet\nabla)\vec{u}(x,y,z,t) = -\nabla p + \nabla^2\vec{u} + \mathcal{R}T\hat{z} \tag{2.7}$$

$$\nabla\bullet\vec{u} = 0 \tag{2.8}$$

$$(\partial_t + \vec{u}\bullet\nabla)T(x,y,z,t) = \nabla^2 T \tag{2.9}$$

where ∂_t is the time derivative, and $\vec{u}$, T, and p are the velocity, temperature, and pressure fields, respectively, as a function of cartesian coordinates (x, y, z) and of time t. Equations (2.7)-(2.9) are known as the Boussinesq equations. The Prandtl number σ is defined as

$$\sigma = \frac{\nu}{\kappa}. \tag{2.10}$$

Equations (2.7)-(2.9) are non-dimensionalized by the vertical thermal diffusion time, d^2/κ, *i.e.* the amount of time it takes for heat to travel across the depth of the domain, d.

The boundary conditions for this problem are as such: A no-slip boundary condition is imposed for the velocity field $\vec{u}$ along all walls of the non-moving domain,

$$\vec{u} = 0. \tag{2.11}$$

For the temperature field, conducting surfaces are selected for the boundary condition along the sidewalls of the domain,

$$T(z) = 1 - z \tag{2.12}$$

with fixed temperatures T_h and T_c at the top and bottom surfaces. The initial temperature fields adhere to Eq. (2.12) with superimposed random thermal perturbations to break symmetry in the problem. Since there is no dynamical equation for pressure it does not require boundary conditions.

2.3.2 Chaos in both space and time

The spirals and defect patterns that emerge in the complex flow regime of spatially-extended systems are characteristic of spatiotemporal chaos, *i.e.* chaos not only temporally but spatially as well. Many techniques have been developed to quantify temporally chaotic dynamics since the phenomenon was first identified in Edward Lorenz's now seminal paper on aperiodic dynamics in a deterministic system [21]. Since then, temporal chaos has been identified and studied in simple mathematical models [24] and experimental systems alike. In fact, a period doubling cascade to chaos was identified in Rayleigh-Bénard experiments with mercury [20]. The methods that have been developed to quantify these dynamics are based on Lyapunov exponents which quantify separation of trajectories in phase space [43]. Using Lyapunov and phase space diagnostics have been particularly useful for analyzing experimental evidence since one is able to reconstruct attractors by using time series signals. However, although these methods are useful for quantifying low-dimensional systems, more work needs to be done to use these tools to explore high-dimensional, spatially complex systems. Only recently have developments been made to explore and quantify these far-from-equilibrium systems. Egolf employed these Lyapunov diagnostics to calculate the fractal dimension of Rayleigh-Bénard convection, *i.e.*, the number of degrees of freedom in a spatially-extended system that contribute to the chaotic dynamics. Their conclusions showed that the chaos was extensive and that the fractal dimension of the system increases linearly with the system volume [10]. The chaotic degrees of freedom were found to correlate with the creation and annihilation of defects in the flow pattern [10]. Karimi and Paul [16] went further and found that the leading order Lyapunov exponent could be used to track topology features in the flow field that contributed to the chaotic dynamics. Their analysis showed that changes from boundary-dominated to bulk-dominated dynamics occur as the system size increased.

2.4 Transport equations

The equations governing the active transport of a species in a flow field is given by the RAD equation,

$$(\partial_t + \vec{u} \bullet \nabla)c = \mathcal{L}\nabla^2 c + Daf(c) \tag{2.13}$$

where c is the concentration field as a function of cartesian coordinates (x, y, z) and time t,

$\mathcal{L}$ is the Lewis number, Da is the Damköhler number, and $f(c)$ is the reaction term that is a function of the concentration field. The Lewis number is defined as the ratio of the molecular to thermal diffusivity,

$$\mathcal{L} = \frac{D}{\kappa}, \tag{2.14}$$

where D is the molecular diffusivity of the tracer used. The Damköhler number is important in measuring the "strength" of the reaction term. Specifically, it is the ratio of the advection to reaction time scales

$$Da = \frac{\tau_V}{\tau_R} \tag{2.15}$$

where τ_V is the advection time scale and τ_R is the reaction time scale. An AD equation can be recovered to model passive transport as the Damköhler number approaches zero due to the reaction time scale approaching infinity.

For the numerical simulations carried out, a simple nonlinear reaction law is selected for the function $f(c)$ that appears in Eq. (2.13). The nonlinearity is named the FKPP reaction term and is similar to the one studied in [1] where the function depends on the concentration of reactants, $(1 - c)$ and products, c. Applying this reaction law, the function $f(c)$ becomes

$$f(c) = c(1 - c). \tag{2.16}$$

The reason for selecting this reaction can be seen by observing its behavior across a range of reactants and products shown in Fig. 2.6. Fig. 2.6 shows that the reaction function $f(c)$ is at a maximum when the concentration of the species is at $c = 0.5$, and is zero at values of $c = 0$ and $c = 1$. This means that no reaction occurs when the concentration field is fully saturated with reactants ($c = 0$) or products ($c = 1$), and that the maximum reaction rate occurs at an equal concentration of reactants and products ($c = 0.5$). This behavior is consistent with the "burn-off" type model that is desired and is similar to physical systems with combustion-like reactions [32].

Another form of the transport equation described in Eq. (2.13) can be formulated to represent an AD system. In this form, the AD equation is non-dimensionalized by the vertical diffusion time of a scalar species, d^2/D, and is represented by

$$(\partial_t + \vec{u} \bullet \nabla)c = \frac{1}{\mathcal{P}}\nabla^2 c. \tag{2.17}$$

By non-dimensionalizing the AD equation by the molecular diffusion time constant, the parameter $\mathcal{P}$ emerges in the equation which is the Péclet number. The Péclet number is a

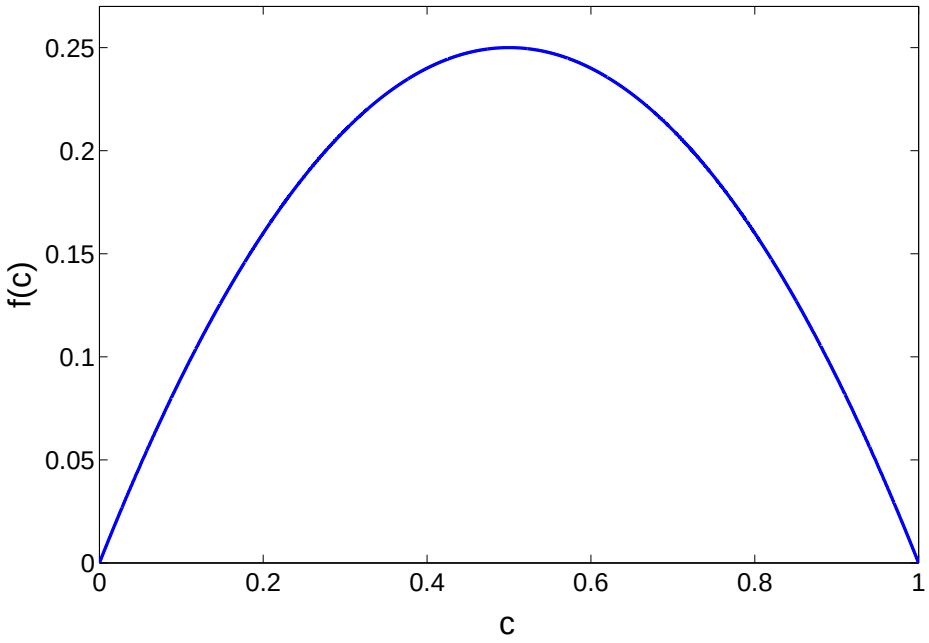

Figure 2.6: The reaction function in the RAD equation used to model the "burn-off" type reaction. In this model, no reaction takes place for saturated values of reactants ($c = 0$) or products ($c = 1$) and reaches a maximum at equal concentrations of reactants and products ($c = 0.5$).

measure of the relative strength of advection of the fluid to the molecular diffusion of the species and is defined as

$$\mathcal{P} = \frac{d||u||}{D}, \tag{2.18}$$

where $||u||$ is the fluid velocity. It can be deduced from the comparison of the Péclet and Lewis numbers that these two parameters are related physically. In fact, the Péclet number is inversely proportional to the Lewis number and they are related by the expression

$$\mathcal{P} = \frac{U}{\mathcal{L}} \tag{2.19}$$

where U is a characteristic fluid speed. Equation 2.13 will be solved simultaneously with Eqs. (2.7)- (2.9) to determine the behavior of the species spreading in the presence of the chaotic flow field. The lateral walls in Fig. 2.4 are chosen to be impermeable to the scalar

species to satisfy the boundary condition,

$$\hat{n} \bullet \nabla c = 0. \tag{2.20}$$

2.5 Experimentally accessible parameter values

The four non-dimensional quantities that govern the physics of the problem at hand are the Rayleigh, Prandtl, Lewis (or Péclet), and Damköhler numbers. The combination of these values create a very large parameter space by which transport may be studied. The goal of this section is to determine the appropriate parameter space that will orientate the numerical results towards those that are experimentally relevant. The factors that dictate the parameter space will be through the combination of values that are experimentally accessible and yield comparable time scales to see the interaction between the three phenomenon: the reacting, diffusing, and advecting time scales.

Experimentally, the values of Lewis numbers that can be investigated are dictated by material properties, namely, the diffusion coefficient of the material used as tracers in experiments. In the experiments carried out in [37] and [38], a particulate impurity (vinyl toluene t-butylstyrene latex spheres) and methylene blue were used as the tracers which have diffusion coefficients of $D = 1.74 \times 10^{-8}$ cm^2/s and $D = 5.7 \times 10^{-6}$ cm^2/s, respectively. The diffusion coefficient in these cases are relatively small values. The corresponding Lewis numbers for this range of diffusion coefficients are $10^{-3} \leq \mathcal{L} \leq 10^{-1}$. These values of Lewis numbers were also investigated in the numerical studies done in [7]. It is in this range of Lewis numbers that one is able to study a range of transport regimes from diffusion-dominated to advective-dominated transport. The corresponding Péclet numbers for this range of Lewis numbers are $10 \leq \mathcal{P} \leq 10^3$.

Typical advection time scales for Rayleigh-Bénard convection are given in Fig. 2.7 for a range of reduced Rayleigh numbers. This thesis is interested in exploring transport in Rayleigh-Bénard convection exhibiting spatiotemporal and spiral defect chaos, a phenomenon which occurs at Rayleigh numbers ranging from $2000 \leq \mathcal{R} \leq 10^4$. In this range of Rayleigh numbers, the advection time scales are in the range of $\tau_V \approx 6$ to $\tau_V \to 0$. Another useful way to quantify the advection time scale is to look at the characteristic non-dimensional speeds across different Rayleigh number flows. Figure 2.8 displays values of characteristic flow speeds as a function of the reduced Rayleigh numbers. For the range of Rayleigh numbers that are of interest, the magnitude of the non-dimensional speed is on the order of $\mathcal{O}(10)$.

Since the Lewis numbers are restricted to values based on what is accessible to experiments, and the Rayleigh numbers are decided to be values that yield spatiotemporal chaos, the Damköhler numbers will be used as the parameter to achieve a balance between the reaction

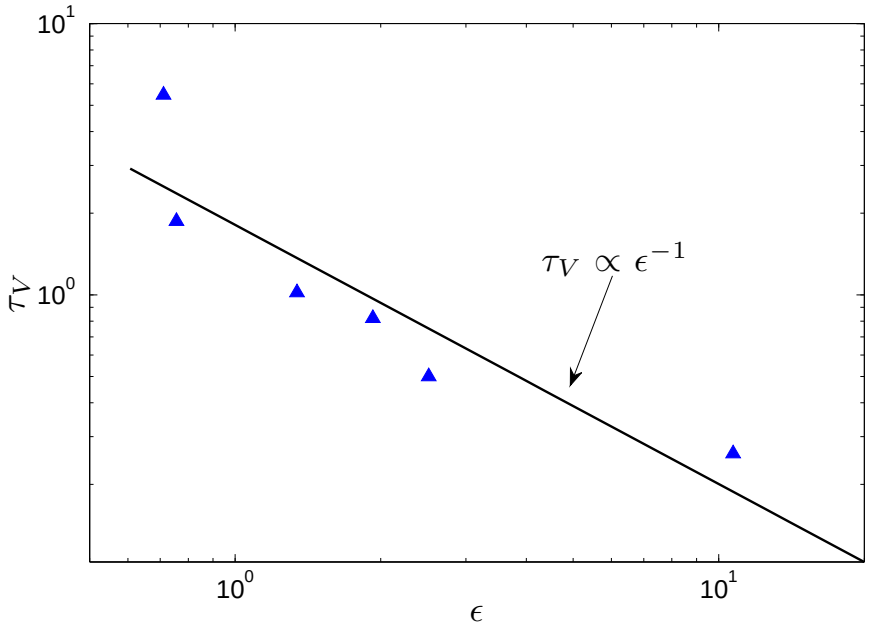

Figure 2.7: Typical advection time scales τ_V for a range of reduced Rayleigh numbers ϵ. The black solid line is a curve fit with a slope equal to -1 on a log-log plot.

time scale and the diffusion and advection time scales. In particular, we would like to achieve a time scale relationship that satisfies the inequality expression

$$\tau_R \leq \tau_V < \tau_D. \tag{2.21}$$

Equation (2.21) signifies that the reaction should be the fastest phenomenon in the problem, or that it should be comparable to the advection time scale. In either case, the diffusion should be the longest phenomenon in the problem in order to model the most physically relevant description. This desired time scale balance is described further in [42].

A description of the time scales in terms of the non-dimensional parameters are needed to be able to satisfy Eq. (2.21). To do so, we first non-dimensionalize the reaction, advection, and diffusion time scales by the vertical diffusion time for heat $\tau = \frac{d^2}{\alpha}$ which yields

$$\tau_R^* = \frac{\tau_R}{d^2/\alpha}, \tag{2.22}$$

$$\tau_V^* = \frac{d^2/\alpha}{d/||u||}, \tag{2.23}$$

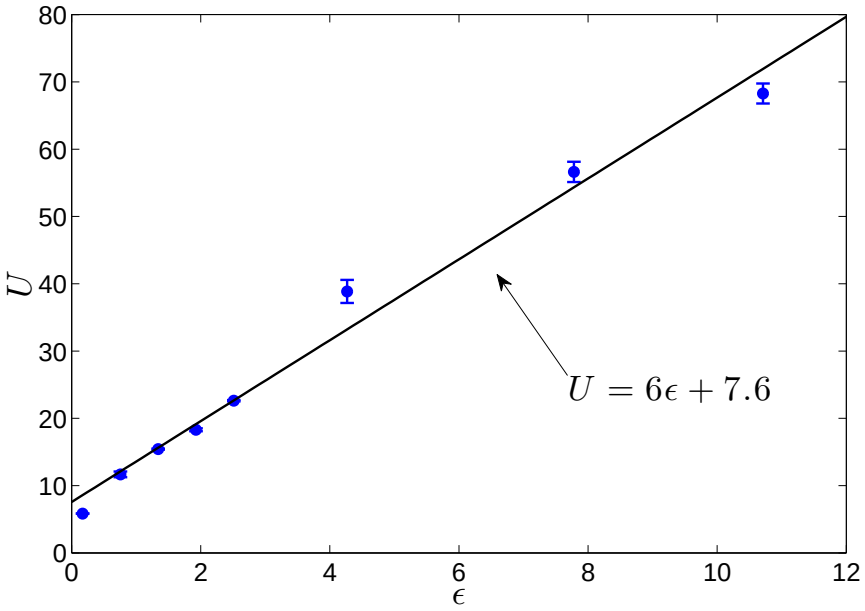

Figure 2.8: Typical characteristic fluid speed U for a range of reduced Rayleigh numbers ϵ for the spatially-extended cylindrical domain investigated. The black solid line is a curve fit with a slope equal to 6.

and

$$\tau_D^* = \frac{d^2/D}{d^2/\alpha} \tag{2.24}$$

where $||u||$ is the magnitude of the fluid velocity. Noting that the non-dimensional, characteristic fluid speed is

$$U = \frac{d}{||u||}, \tag{2.25}$$

we can now use Eqs. (2.22)-(2.24) in conjunction with the definition in Eq. (2.25) to determine the Damköhler numbers necessary to achieve the desired time scale conditions that satisfy Eq. (2.21). By inspection of Fig. 2.8, it is seen that for the Rayleigh numbers of interest the characteristic fluid speed is on the order of $\mathcal{O}(10)$ and therefore the desired reaction time scale should be on the order of $\mathcal{O}(10)$ as well. By using the information about the characteristic fluid speed U and noting that the Lewis numbers are restricted to those that are experimentally accessible, the Damk ohler number range that will satisfy Eq. (2.21)

is

$$0 \leq Da \leq 1. \tag{2.26}$$

One area of active transport that is of importance to the scientific community is the combustion of premixed gases. These type of reactions are generally "fast" compared to the characteristic fluid velocity, and therefore have very large Damköhler numbers. Approximate values of front speed and reaction time scales are given in Table 2.1 for methane and hydrogen. Upon inspection of Table 2.1, it can be seen that the very small reaction time scales yield Damköhler numbers in the range of $1.5 \times 10^4 \leq Da \leq 2.6 \times 10^6$. In this large Damköhler number regime, the transport is reaction-dominated and advection rolls have little effect on the transport of the species.

pre-mixed gas	$\tau_R(s)$	$v_f(m/s)$	Da
CH_4	1.5×10^{-4}	0.4	$\mathcal{O}(10^4)$
H_2	2.6×10^{-6}	3	$\mathcal{O}(10^6)$

Table 2.1: Values of τ_R, v_f, and Da for combustion of methane (CH_4) and hydrogen (H_2).

To summarize, the relevant non-dimensional time scales to the transport problem are listed below as functions of the relevant non-dimensional parameters:

$$\tau_V^* = \frac{1}{U}, \tag{2.27}$$

$$\tau_R^* = \frac{1}{UDa}, \tag{2.28}$$

and

$$\tau_D^* = \frac{1}{\mathcal{L}}. \tag{2.29}$$

Summarized below are the simulations that will be carried out and analyzed in this thesis and the corresponding time scales and non-dimensional parameters. Table 2.2 show the simulations for the $\Gamma = 10$ domain and Table 2.3 show those for the $\Gamma = 40$ domain.

$\mathcal{R}$	τ_V^*	τ_R^*	τ_D^*	$\mathcal{L}$	$\mathcal{P}$	Da
0	N/A	N/A	1.0	10^{-1},10^{-2},10^{-3}	N/A	N/A
2000	5.46	0	1.0	10^{-1},10^{-2},10^{-3}	$10^1, 10^2, 10^3$	0
3000	1.87	0	1.0	10^{-1},10^{-2},10^{-3}	$10^1, 10^2, 10^3$	0
4000	1.02	0	1.0	10^{-1},10^{-2},10^{-3}	$10^1, 10^2, 10^3$	0
5000	0.82	0	1.0	10^{-1},10^{-2},10^{-3}	$10^1, 10^2, 10^3$	0
6000	0.5	$0, 5, 0.5$	1.0	10^{-1},10^{-2},10^{-3}	$10^1, 10^2, 10^3$	$0, 10^{-1}, 1$

Table 2.2: List of simulations for $\Gamma = 10$

$\mathcal{R}$	τ_V^*	τ_R^*	τ_D^*	$\mathcal{L}$	$\mathcal{P}$	Da
0	N/A	N/A	1.0	10^{-1}	N/A	N/A
2000	5.46	0.29	1.0	10^{-1}	10^1	$0, 1/2, 1$
4000	1.02	7.18×10^{-3}	1.0	10^{-1}	10^1	$0, 1/2, 1$
6000	0.5	4.23×10^{-3}	1.0	10^{-1}	10^1	$0, 1/2, 1$
20000	0.26	2.13×10^{-4}	1.0	10^{-1}	10^1	$0, 1/2, 1$

Table 2.3: List of simulations for $\Gamma = 40$

2.6 Direct numerical simulations

The simulations were carried out using the open source solver Nek5000. The Boussinesq equations in Eqs. (2.7)-(2.9) and the reaction-advection-diffusion equation in Eq. (2.13) are simultaneously integrated using a parallel spectral element approach. The localized gaussian distribution is selected for the initial condition of the scalar species such that

$$c\left(x, y, z, t = 0\right) = \exp\left(-\frac{x^2 + y^2 + z^2}{2\Delta^2}\right), \tag{2.30}$$

where $\Delta = 1/2$. The initial conditions used for the Boussinesq equations are temperature, pressure and velocity fields that have been "warmed-up" from initial random thermal perturbations for a total of $t = 100$ and $t = 1600$ time units for the $\Gamma = 10$ and $\Gamma = 40$ domains, respectively, in order to decay any transient effects in the flow field. These warm-up times were derived from the fact that it takes one time unit for heat to travel a distance, d, from the bottom to the top of the domain. Therefore, it is assumed that any transient effects in the flow field can be neglected after a time of $\mathcal{O}(\Gamma^2)$ needed for heat to travel across the area of the domain.

Spectral element methods are similar to finite element methods in that they utilize a similar discretization scheme to yield high-order accurate solutions. The spectral element method differs from the finite element method in the orthogonality of the basis functions used. In the latter method, orthogonality is due to the use of nonoverlapping local functions as the basis functions. In spectral methods, Legendre polynomials are used as the basis functions across the domain, which is why it lends itself as a global method [9]. Nek5000 is specifically designed to solve the incompressible Navier-Stokes equations for a variety of boundary conditions. One advantage of employing this spectral element method is that large scale parallel computations can be done efficiently and with exponential convergence in space. The solver is capable of using a second or third order accurate Adams-Bashforth time step. Unless otherwise noted, the simulations are carried out with each element using $n = 11$ polynomial interpolating nodes. The solution procedure and more information about the Nek5000 solver can be found in [13]. The original source code for the solver integrates the mass, momentum, energy and the advection-diffusion equation in three-dimensions. Modifications to the code allow for the explicit solution of a reaction term in the transport equation. Because of employing this explicit approach, very high Damköhler numbers, like those found in the combustion of pre-mixed gasses, are not accessible through the current numerical scheme. Additionally, as can be seen in Table 2.3 that adding an explicit reaction term limits the ability to explore the low Lewis number transport regime (i.e. $\mathcal{L} = 10^{-2}$ and $\mathcal{L} = 10^{-3}$), so for the active transport simulations, only Lewis numbers at $\mathcal{L} = 10^{-1}$ are explored.

Nek5000 was created for a parallelized computer architecture and it has been shown to scale to over a million processors for some computational problems [40]. However, scaling to a large number of processors does not necessarily scale the performance. At some point the communication cost within the parallel architecture overcomes the savings in computation time. Figure 2.9 summarizes the speedup study using Nek5000 for a domain size $\Gamma = 40$ at a Rayleigh number $\mathcal{R} = 9000$. There is a dramatic increase in performance by scaling from 64 to 128 processors; however, this gain in performance diminishes and plateaus past 128 processors which suggests it is at this number the simulations should be run.

The spectral element meshes constructed for the $\Gamma = 10$ and $\Gamma = 40$ domains that are used for the simulations are shown in Fig. 2.10 and Fig. 2.11, respectively.

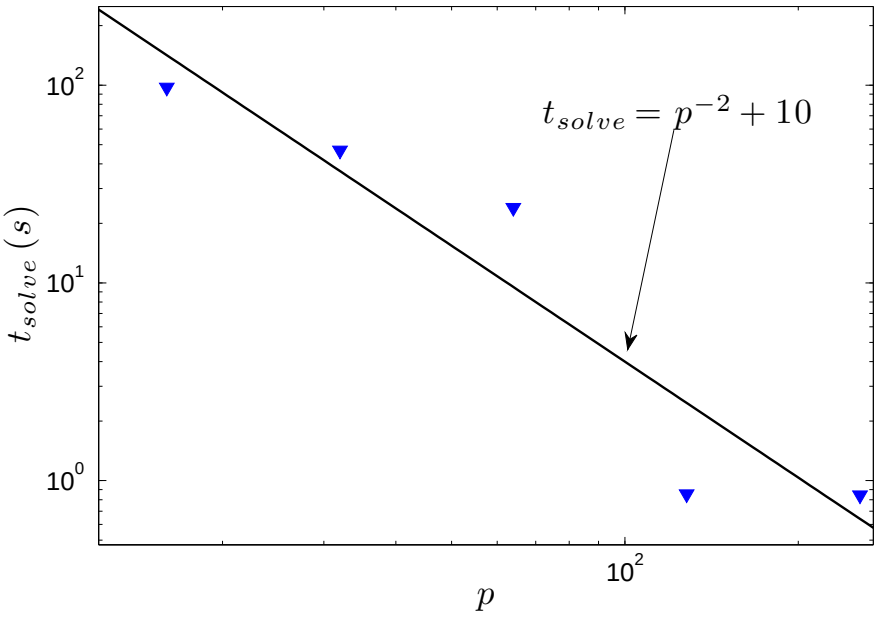

Figure 2.9: Average computation time required to advance one time step t_{solve} as a function of the number of cores p employed in the job batch. The test case was run for a $\Gamma = 40$ domain with 3072 elements with $n = 11$ order polynomial. The black solid line is a curve fit with a slope of -2.

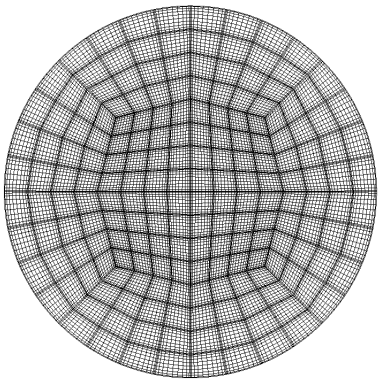

Figure 2.10: Mesh of 192 spectral elements used for $\Gamma = 10$.

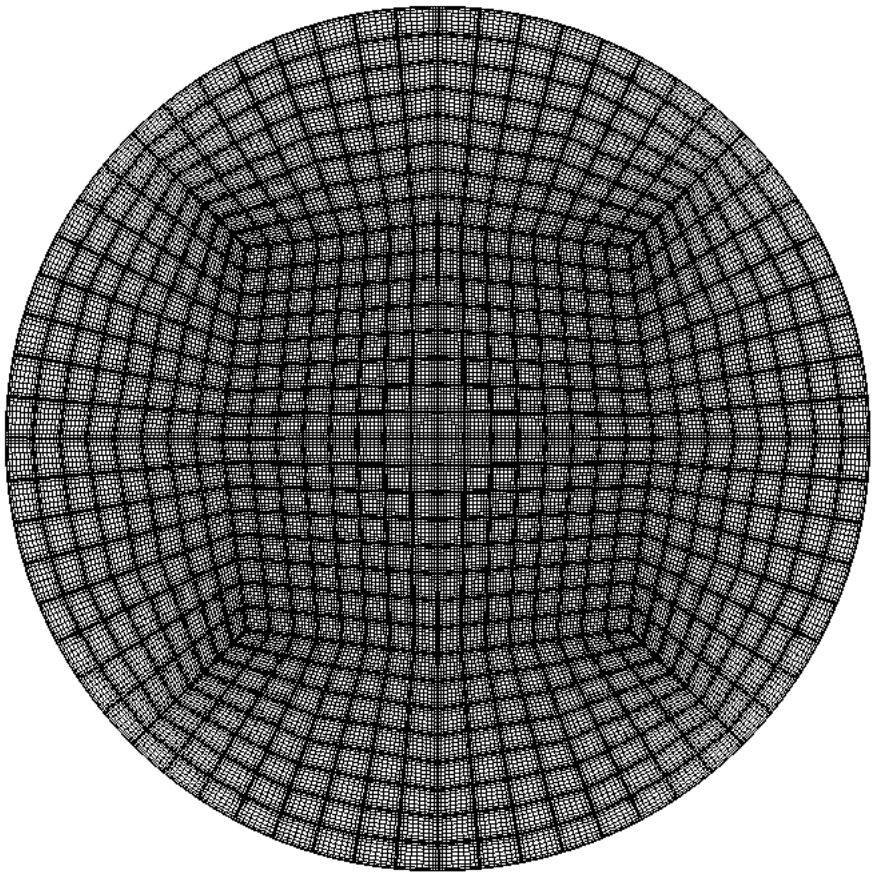

Figure 2.11: Mesh of 3072 spectral elements used for $\Gamma = 40$.

Chapter 3

Results

In this chapter, the results of the simulations will be presented. A discussion of the diagnostic tools used to quantify transport will follow and the application of these diagnostics to the results will be presented.

3.1 Simulation results

3.1.1 Flow fields

The flow fields for $\Gamma = 10$ and $\Gamma = 40$ are presented in Figs. 3.1-3.2. The flow field is represented by the midplane temperature where the red indicates hot rising fluid and the blue represents cold sinking fluid. For the $\Gamma = 10$ domain, the flow field is time-independent for $\mathcal{R} = 2000$ ($\epsilon = 0.17$) consisting of parallel convection rolls with a few defects located at either corner of the domain. Figure 3.1(a) depicts this case. For Rayleigh numbers greater than $\mathcal{R} = 2000$ ($\epsilon = 0.17$), the flow becomes complex and transitions from time-independent to time-dependent patterns described by many defects traveling across the flow field solution. These conditions are present in the flow fields pictured in Fig. 3.1(b)-3.1(e).

The midplane temperature patterns for $\Gamma = 40$ are shown in Fig. 3.2. The first difference between these patterns to those of $\Gamma = 10$ is with the stable solution at $\mathcal{R} = 2000$ ($\epsilon = 0.17$). Figure 3.2(a) shows that at this Rayleigh number, the stable solution produced is a series of steady concentric convection rings that form a target pattern. As the Rayleigh number is increased, the pattern breaks down into an unstable time-dependent pattern that is characterized as spiral defect chaos. These types of patterns are depicted in Figs. 3.2(b)-(d). As the Rayleigh number is increased further, the convection rolls exhibit a lateral oscillatory instability, as seen in the solutions in Fig. 3.2(e) and Fig. 3.2(f), that is characteristic of plume formation in turbulent flows. These lateral oscillations in the flow fields exist when solved with higher-order polynomials, which suggest that they are not attributed to

numerical noise, but instead due to the convection pattern undergoing an instability.

These flow fields were used as the initial pressure, temperature and velocity fields for the evolution of the transport simulations described in the next section.

3.1.2 Passive transport

The set of images shown in Fig. 3.3 display the time evolution of a passive scalar species with a Lewis number $\mathcal{L} = 10^{-2}$ within a flow field with Prandtl number $\sigma = 1$ and Rayleigh number $\mathcal{R} = 6000$ ($\epsilon = 2.51$). The domain size used for the passive transport simulations was $\Gamma = 10$. The black contour lines represent midplane ($z = 0.5$) temperature values that roughly correspond to the boundaries between convection rolls. The colors in the plots indicate the level of concentration of the species with red indicating the highest concentration and blue indicating a concentration of zero. The scalar spreading progresses from an initial condition $t = 0$ as shown in Fig. 3.3(a) to a final time at $t = 50$ shown in Fig. 3.3(f). At each time the scale for the species concentration changes in order to visualize the spreading and therefore should not be mistaken as the presence of a species source within the system. Figure 3.3(b) shows transport of the species occurring parallel to the convection roll while maintaining a local distribution. At later times, as shown in Fig. 3.3(c)-(e), the species begins to diffuse across the convection rolls and spreads across the domain until it saturates at about time $t = 50$ as shown in Fig. 3.3(f).

3.1.3 Active transport

A sample result of active transport governed by a nonlinear FKPP reaction term is presented in Fig. 3.4 for a Prandtl number $\sigma = 1$ and Rayleigh number $\mathcal{R} = 6000$ ($\epsilon = 2.51$) and $\Gamma = 40$. The Lewis number of the species is $\mathcal{L} = 10^{-1}$. The midplane temperature contours are represented by the black lines with with color representing the concentration of the active species. In these plots, the red represents the presence of products ($c = 1$) and the blue represents the absence of products ($c = 0$). The spreading begins from an initial Gaussian distribution in Fig. 3.4(a) at $t = 0$ to a complete saturation of products across the domain as shown in Fig. 3.4(f) at around time $t = 20$. Many interesting features can be seen the time evolution of the reaction. One feature is the enhanced spreading of the reacting species that occurs significantly at times of $t < 10$ as seen in Fig. 3.4(b) and Fig. 3.4(c). This enhanced spreading orientation is not seen at later times of the species evolution where the reaction front begins to advance in all directions uniformly. The other important feature to note is the fractal-like front structure that emerges in the presence of the flow field. This may be an indication of a reaction enhancement taking place due to an increase in the surface area boundary between reactants and products. Methods to quantify this enhancement will be discussed in the following sections. Figure 3.5 shows the evolution of a reaction within a $\mathcal{R} = 2000$ flow field at $\Gamma = 40$, $\sigma = 1$, and $\mathcal{L} = 10^{-1}$. Within this region, the flow field

is characterized by a time-independent target pattern which is analogous to other systems of two-dimensional chain of time-independent vortices that were discussed in Section 2.2. Figure 3.6 shows a cross-sectional view of the reaction from an intersection of the $x = 0$ plane. These images are taken are a smaller subsection of the $\Gamma = 40$ domain to better visualize the spreading.

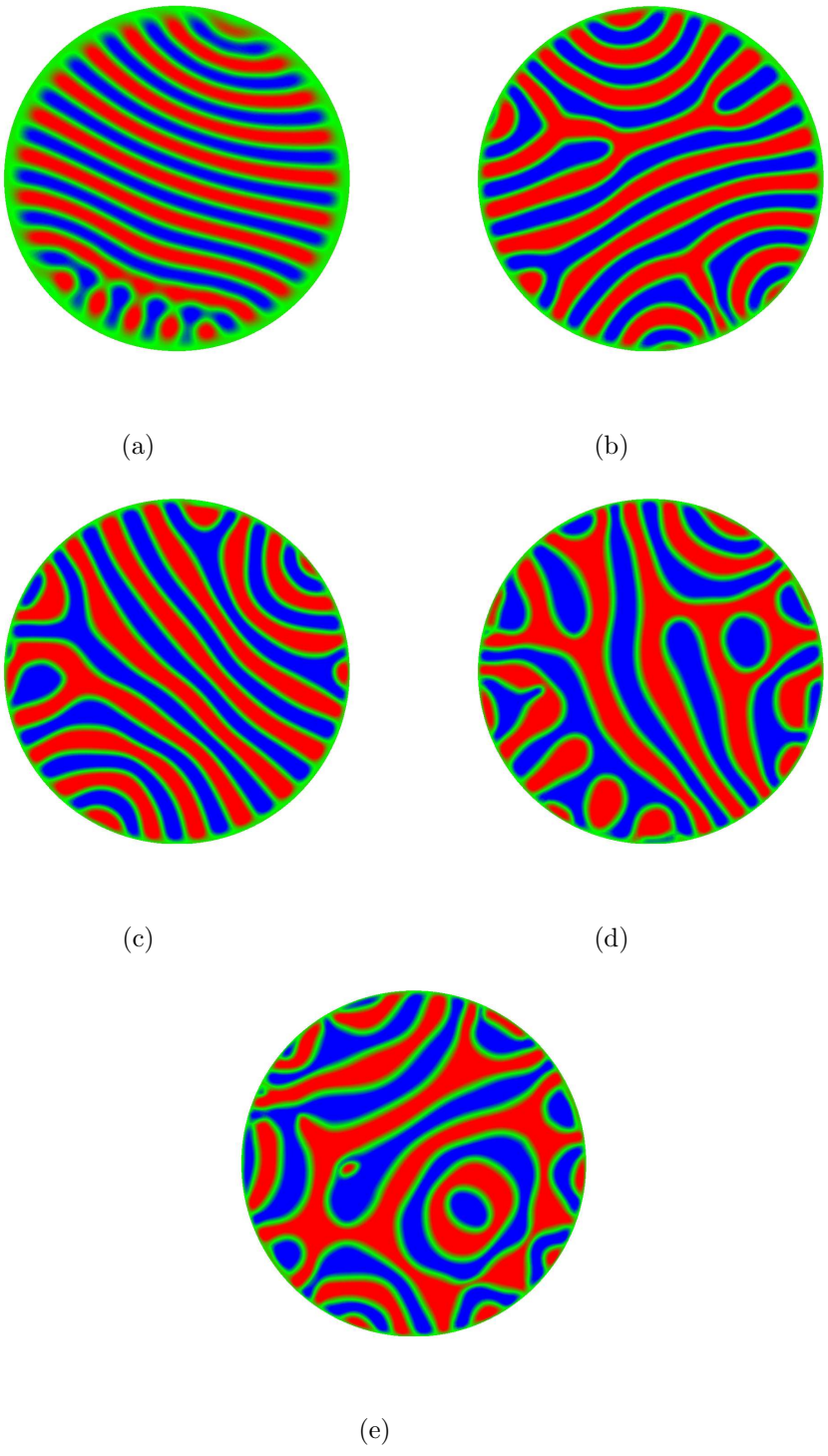

Figure 3.1: $\Gamma = 10$ temperature fields at the midplane location $z = 0.5$ for Rayleigh numbers (a) $\mathcal{R} = 2000$ ($\epsilon = 0.17$), (b) $\mathcal{R} = 3000$ ($\epsilon = 0.76$), (c) $\mathcal{R} = 4000$ ($\epsilon = 1.34$), (d) $\mathcal{R} = 5000$ ($\epsilon = 1.93$), and (e) $\mathcal{R} = 6000$ ($\epsilon = 2.51$). Red represents hot rising fluid while blue represents cold sinking fluid. Qualitatively, the complexity of the convection roll pattern increases as the Rayleigh number increases.

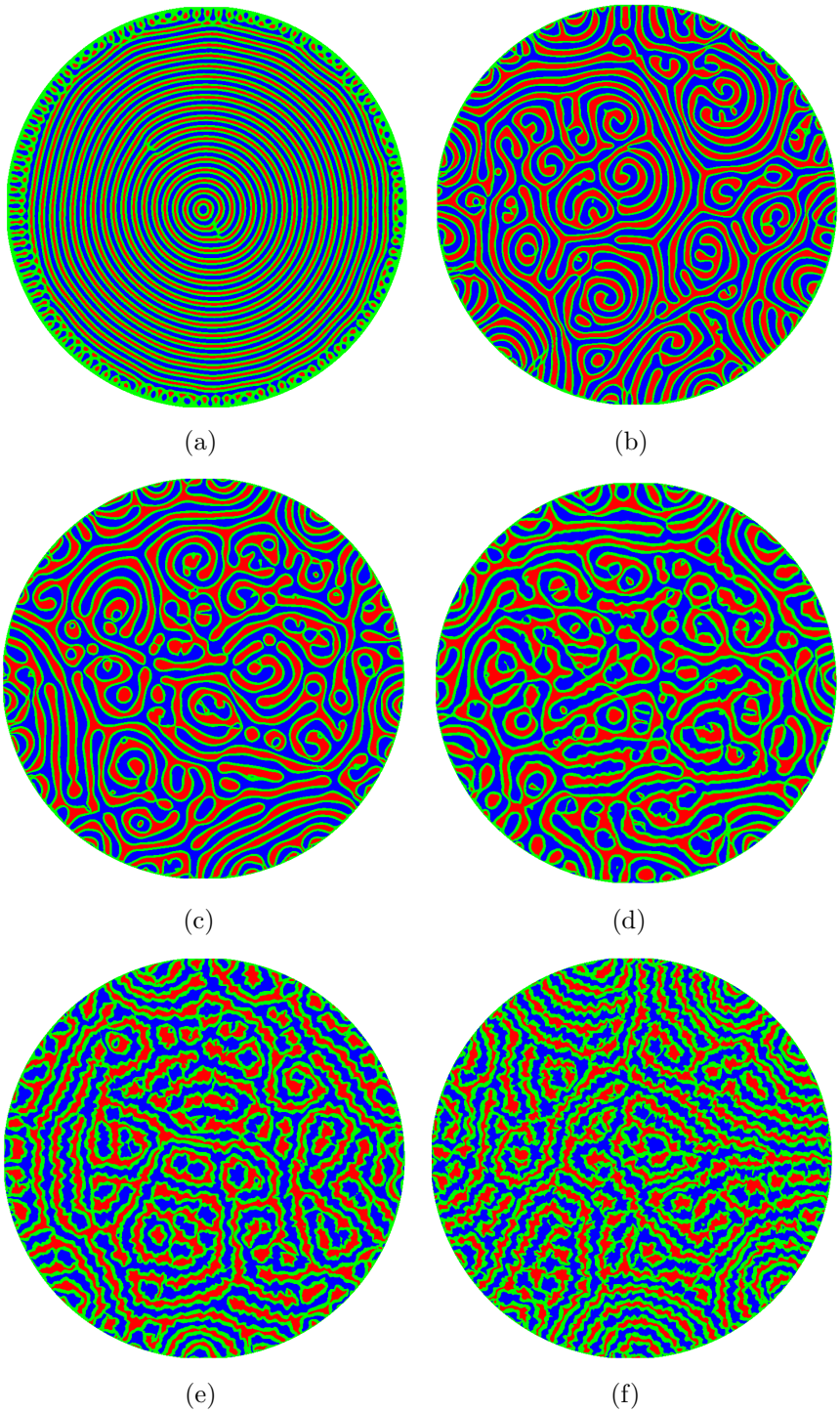

Figure 3.2: $\Gamma = 40$ temperature fields at the midplane location $z = 0.5$ for Rayleigh numbers (a) $\mathcal{R} = 2000$ ($\epsilon = 0.17$), (b) $\mathcal{R} = 4000$ ($\epsilon = 1.34$), (c) $\mathcal{R} = 6000$ ($\epsilon = 2.51$), (d) $\mathcal{R} = 9000$ ($\epsilon = 4.27$), (e) $\mathcal{R} = 15000$ ($\epsilon = 7.78$) and (f) $\mathcal{R} = 20000$ ($\epsilon = 10.71$). Red represents hot rising fluid while blue represents cold sinking fluid. Similar to the $\Gamma = 10$ flow fields, the complexity of the convection roll pattern increases as the Rayleigh number increases.

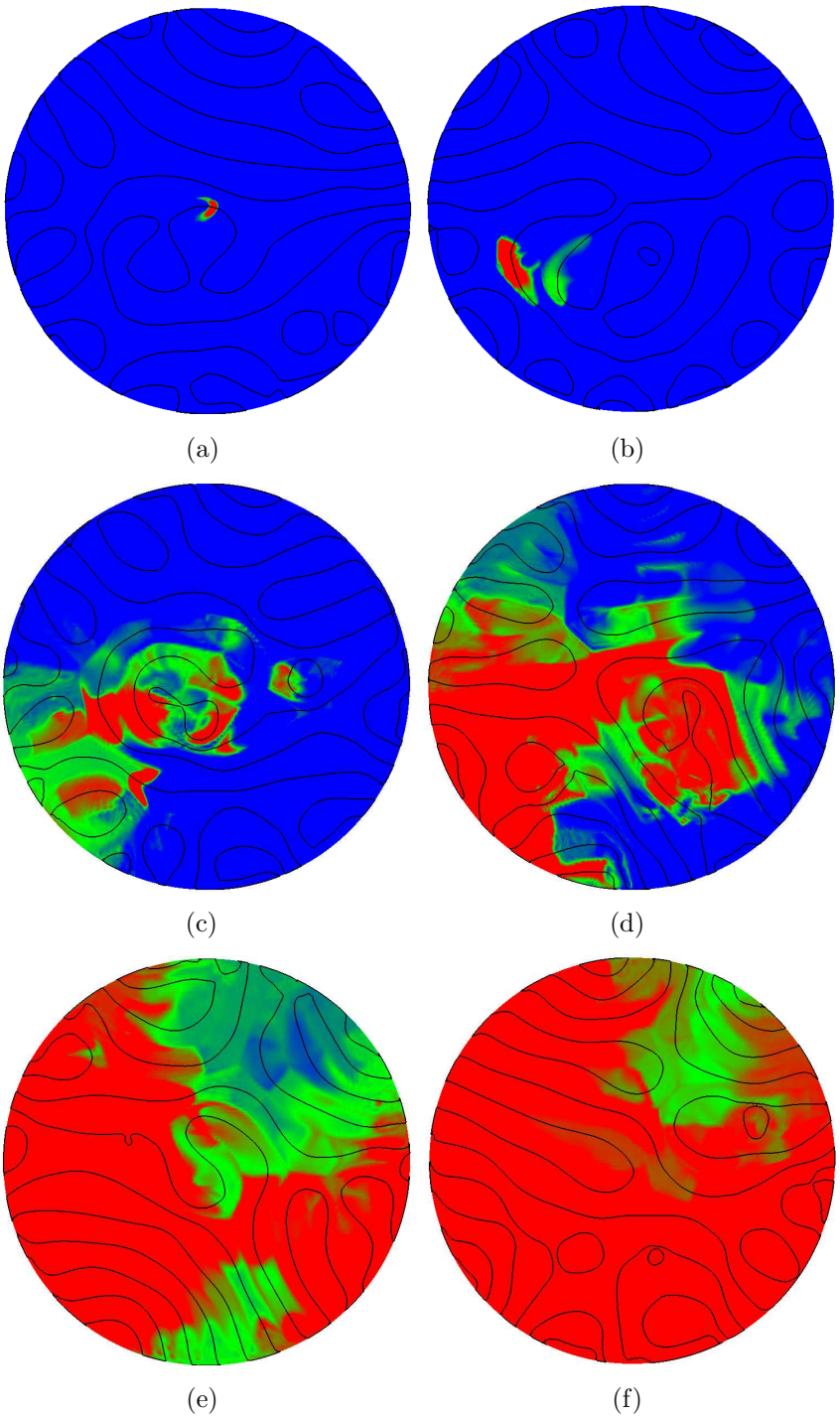

Figure 3.3: Transport of a passive scalar species for $\Gamma = 10$, $\mathcal{R} = 6000$ and $\mathcal{L} = 10^{-2}$. Each figure represents the passive species concentration at times (a) $t = 0$, (b) $t = 10$, (c) $t = 20$, (d) $t = 30$, (e) $t = 40$, and (f) $t = 50$. In these figures the high concentrations are indicated by red and zero concentration indicated by blue. The midplane temperature solution for $T = 0.5$ are indicated by the black contour lines to visualize the convection rolls.

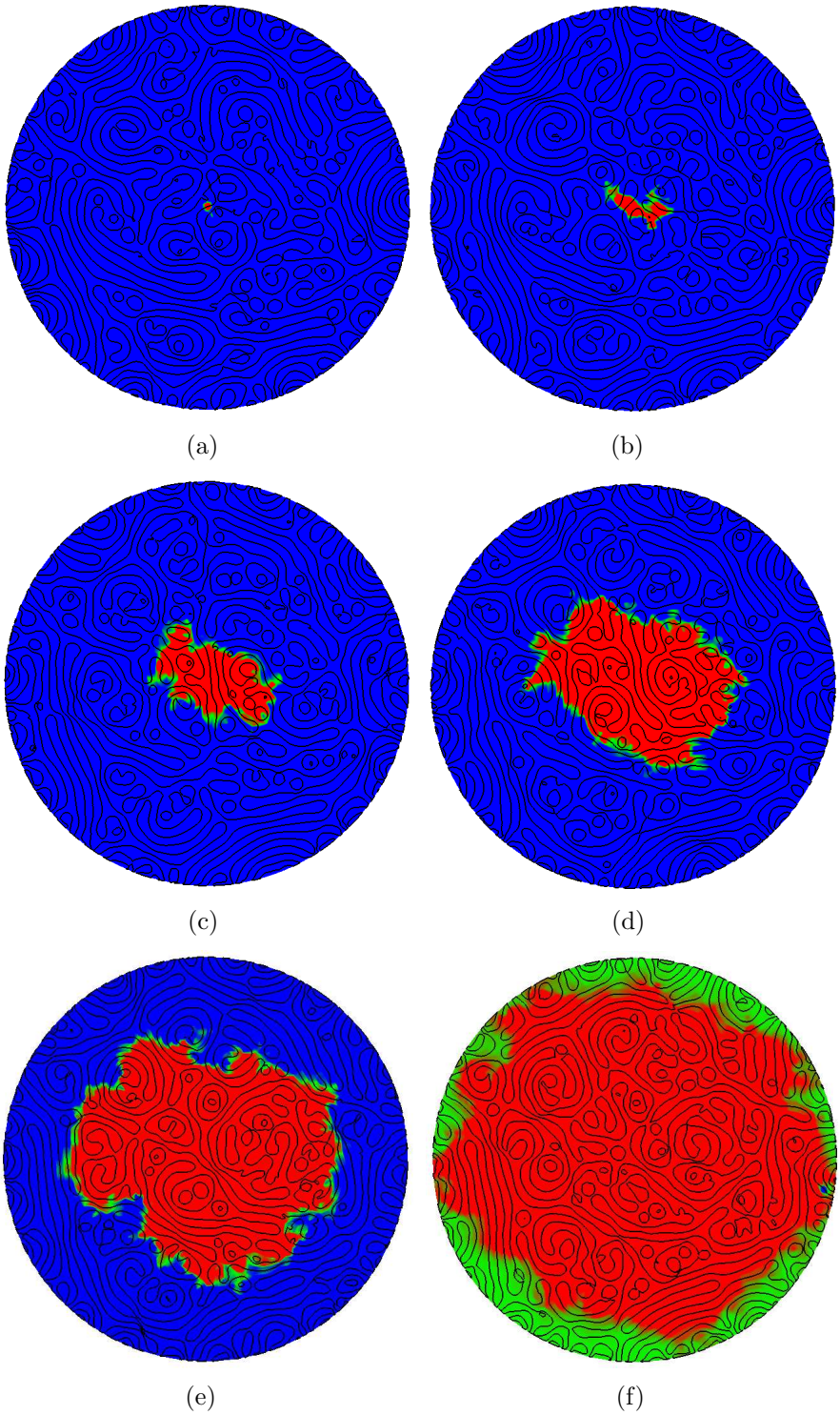

Figure 3.4: Active transport for $\Gamma = 40$, $\mathcal{R} = 4000$, $\mathcal{L} = 10^{-1}$, and $Da = 1/2$ at times (a) $t = 0$, (b) $t = 4$, (c) $t = 8$, (d) $t = 12$, (e) $t = 16$, and (f) $t = 20$. In these images the products of the reaction are indicated as red and the reactants as blue. The midplane temperature solution for $T = 0.5$ are indicated by the black contour lines to visualize the convection rolls.

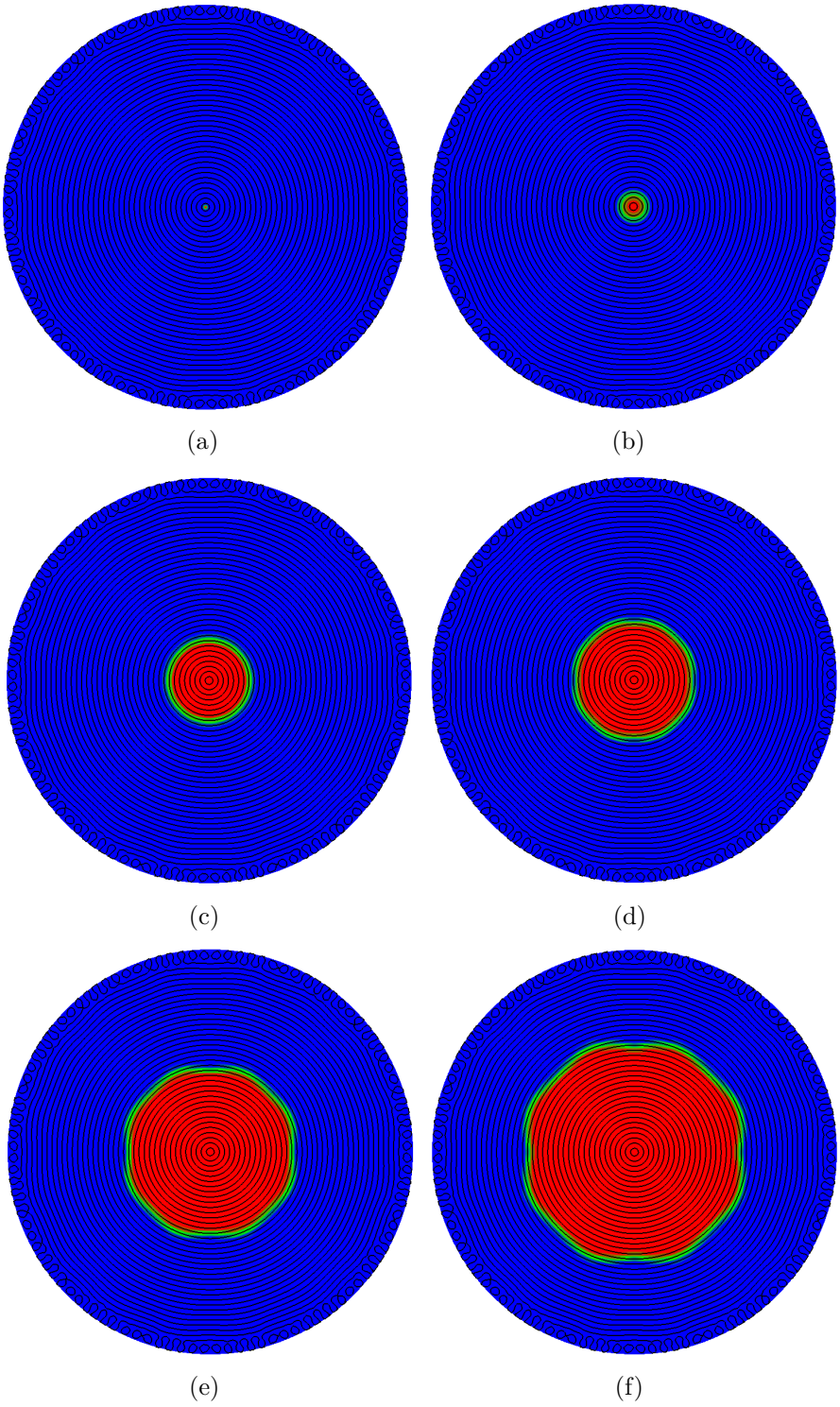

Figure 3.5: Active transport for $\Gamma = 40$, $\mathcal{R} = 2000$, $\mathcal{L} = 10^{-1}$, and $Da = 1$ at times (a) $t = 0$, (b) $t = 4$, (c) $t = 9$, (d) $t = 12$, (e) $t = 16$, and (f) $t = 20$. In these images the products of the reaction are indicated as red and the reactants as blue. The midplane temperature solution for $T = 0.5$ are indicated by the black contour lines to visualize the convection rolls.

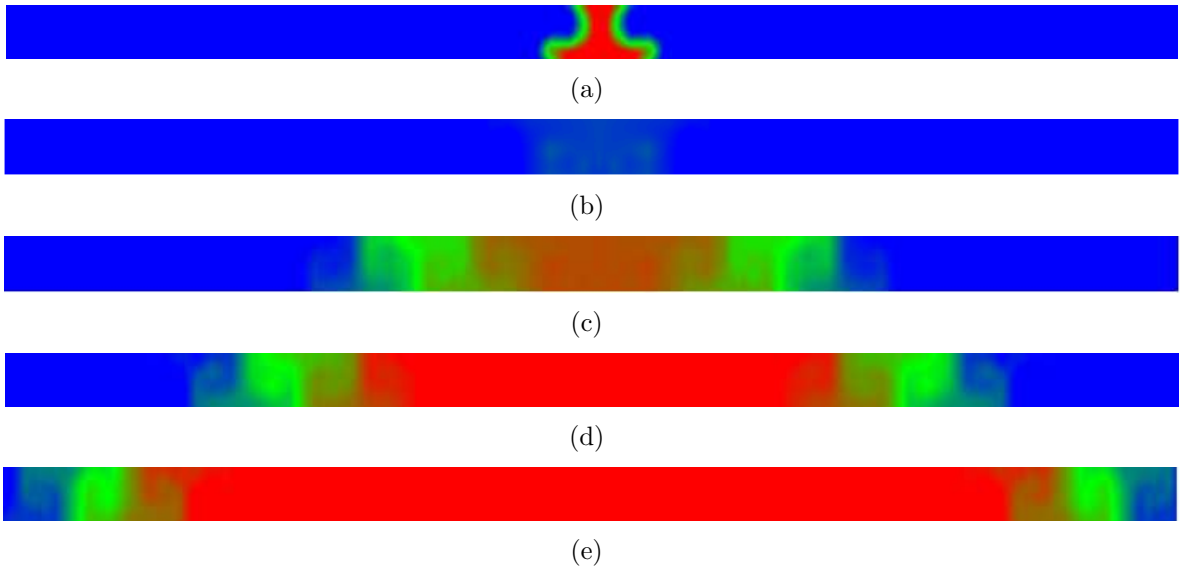

Figure 3.6: Vertical cross-section of the reaction for the same parameters as those in Fig. 3.5 for times (a) just after $t = 0$, (b) $t = 4$ (c) $t = 9$ (d) $t = 12$ and (e) $t = 16$. Only half of the domain is shown in the figures above to better visualize the details of the spreading.

3.2 Diagnostics

There are many ways to quantify the transport of species within a spatially-extended domain. In this section, these methods will be described and applied to the results from the numerical simulations. The transport of the species is analyzed as a two-dimensional spreading process due to the large aspect ratio domain studied.

3.2.1 Statistical moments

One way to study the transport of a species is to quantify the spreading globally by calculating the mean-square displacement over time. Since the domains investigated have large-aspect ratios, the statistics of the spreading of the species can be quantified in two dimensions. The mean-square displacement in cylindrical coordinates is represented as

$$V(t) = \frac{\int_0^{\Gamma} \int_0^{2\pi} \left[r - \bar{r}\,(t)\right]^2 c\,(r,\theta,t)\, r dr d\theta}{\int_0^{\Gamma} \int_0^{2\pi} c\,(r,\theta,t)\, r dr d\theta} \tag{3.1}$$

where the quantity $\bar{r}\,(t)$ is the area-averaged species concentration field and is defined as

$$\bar{r}\,(t) = \frac{\int_0^{\Gamma} \int_0^{2\pi} r c\,(r,\theta,t)\, r dr d\theta}{\int_0^{\Gamma} \int_0^{2\pi} c\,(r,\theta,t)\, r dr d\theta}. \tag{3.2}$$

The mean-square displacement was numerically integrated for each of the simulations. Figure 3.7 shows the mean-square displacement over time for passive transport in a flow field with $\mathcal{R} = 3000$ ($\epsilon = 0.17$), $\mathcal{L} = 10^{-1}$, $\mathcal{L} = 10^{-2}$, and $\mathcal{L} = 10^{-3}$. The mean-square displacement grows proportional to time with a power law $\gamma \approx 1$. These results have also been documented in [7] for numerical simulations in chaotic flow fields. Since the growth of the mean-square displacement over time time follows a unity power law, that is,

$$V\,(t) \propto t^{\gamma} \tag{3.3}$$

where $\gamma = 1$, the spreading can be described as an overall normal diffusion process and the averaged spreading of the species, $\tilde{c}\,(t)$, can be described by a reduced one-dimensional diffusion process governed by

$$\partial_t \tilde{c}\,(r,t) = \mathcal{L}^* \partial_{rr} \tilde{c} \tag{3.4}$$

where $\mathcal{L}^*$ is the effective Lewis number – in other words, the effective Lewis number captures the contributions of convection into the transport equation. This value can be extracted

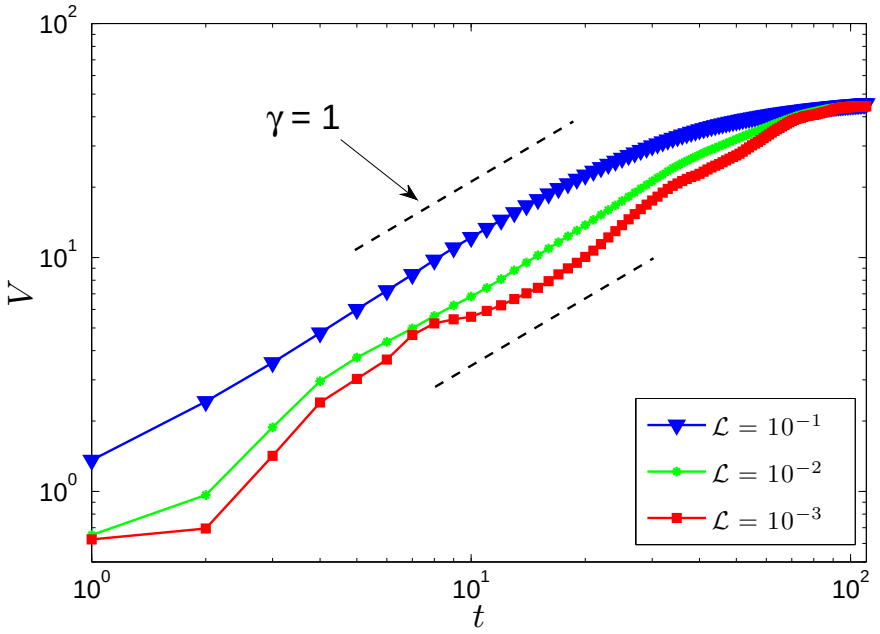

Figure 3.7: The mean-square displacement V as a function of time t for passive transport for $\Gamma = 10$ and $\mathcal{R} = 3000$. The mean-square displacement grows proportionally with time following a power law $\gamma = 1$ for all Lewis numbers $\mathcal{L} = 10^{-1}$, $\mathcal{L} = 10^{-2}$, and $\mathcal{L} = 10^{-3}$. The deviation of the trend at large times is due to finite wall effects for $\Gamma = 10$.

from the mean-square displacement by the equation,

$$V(t) = 4\mathcal{L}^* t. \tag{3.5}$$

Another test that can be done to confirm that the averaged spreading is a normal diffusive process is to look at the ratio of higher-order moments to the mean-square displacement. For normal diffusive processes, the higher-order moments should scale

$$M_q(t) \propto t^{\frac{q}{2}} \tag{3.6}$$

where q is an integer of higher order moments and M_q is the higher-order moment defined as

$$M_q(t) = \frac{\int_0^{\Gamma}\int_0^{2\pi} [r - \bar{r}(t)]^q \, c(r,\theta,t)\, r dr d\theta}{\int_0^{\Gamma}\int_0^{2\pi} c(r,\theta,t)\, r dr d\theta}. \tag{3.7}$$

Notice that when $q = 2$, the definition of the mean-square displacement $V(t)$ in Eq. (3.1) is recovered. The ratio of this higher-order moment with the mean-square displacement should

then be constant in time for normal diffusive processes. Plotted in Fig. 3.8 are ratios of higher-order moments for $q = 4, 6$, and 8. Each of the higher-order moment ratios approach a constant value over time which confirm that normal diffusion is occurring.

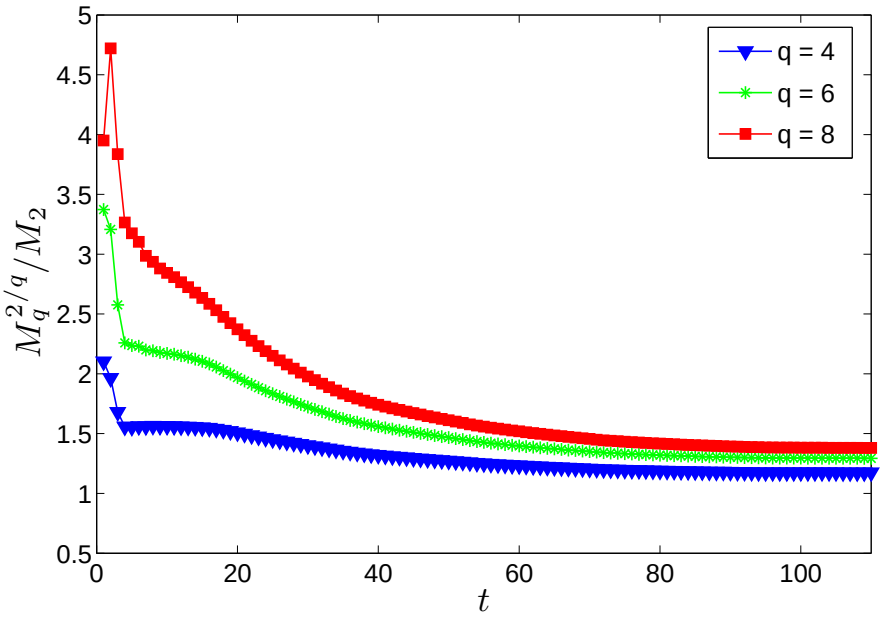

Figure 3.8: Ratio of higher-order moments $M_q(t)^{2/q}$ to the mean-square displacement M_2 as a function of time t for values of $q = 4$, $q = 6$, and $q = 8$. The leveling off of $M_q(t)^{2/q}/M_2$ over a certain time interval suggests a normal diffusion process.

3.2.2 Transport enhancement due to spatiotemporal chaos

One way to quantify transport enhancement is to quantify the difference between the effective Lewis number $\mathcal{L}^*$ and the Lewis number $\mathcal{L}$ in order to isolate effects of the convection on the overall diffusive process. The non-dimensional transport enhancement factor is defined as

$$\Delta = \frac{\mathcal{L}^* - \mathcal{L}}{\mathcal{L}}. \tag{3.8}$$

Distinct enhancement regimes emerge when the transport enhancement factor is plotted as a function of the Péclet number of the flow. Figure 3.9 highlights the appearance of these two transport regimes: a diffusion-dominated and an advection-dominated regime that occur as a result of the presence of the complex flow field. These regimes depend on the relative strength of the advecting fluid therefore by describing the transport enhancement factor as a function of the Péclet number, the two regimes may be described based on the relative importance of

advection and diffusion in the problem. For diffusion-dominated transport that occurs in the low Péclet number regime, the transport enhancement factor is proportional to Péclet number by $\Delta \propto \mathcal{P}^{1/2}$. At a certain Péclet number, the transport becomes advection-dominated and the scaling law that the transport enhancement factor follows becomes $\Delta \propto \mathcal{P}$. It is unclear yet whether this transition between the two scaling regimes is gradual or an abrupt transition. However, these two transport enhancement regimes are in agreement with those found in experiments of passive tracers in time-independent [37] and time-dependent flow fields [37] as well as in numerical simulations of spiral defect chaos [7].

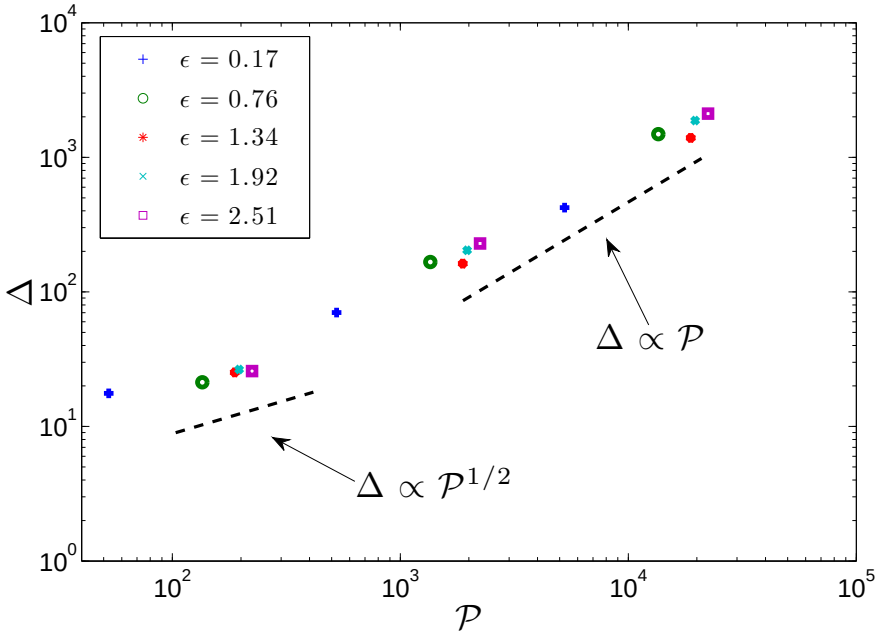

Figure 3.9: Transport enhancement Δ of a passive species as a function of the Péclet number, $\mathcal{P}$ for $\Gamma = 10$. Two distinct transport enhancement regimes occur for diffusion-dominated and advective-dominated transport which scale by $\mathcal{P}^{1/2}$ and $\mathcal{P}$, respectively.

3.2.3 Anomalous diffusion for nonlinear reactions

It can be seen from the preceding section that when the spreading of the species follows a normal diffusion process, quantifying transport enhancement can be done relatively easily by extracting an overall diffusion coefficient from the mean-square displacement. This procedure cannot be used when the diffusive behavior is anomalous – that is, the mean-square displacement follows the trend described by Eq. (3.3) with an exponent $\gamma \neq 1$. As will be seen, transport involving nonlinear reactions like FKPP reaction studied in this thesis subscribe to this type of anomalous behavior.

Figure 3.10 displays the mean-square displacement over time for $\mathcal{R} = 6000$ and $Da =$

0 (*passive*), $Da = 1$ and $Da = 10$. The results show that for $Da = 0$, the transport recovers the normal diffusive process with $\gamma = 1$ as seen in the previous section. However, for active transport with $Da > 0$, the mean-square displacement exhibits $\gamma > 1$ indicating a superdiffusive process. Additionally, the finite wall effects of the $\Gamma = 10$ domain are more pronounced in the spreading of the active species. It is for this reason that the transition to transport simulations were conducted in $\Gamma = 40$ to better quantify the spreading dynamics.

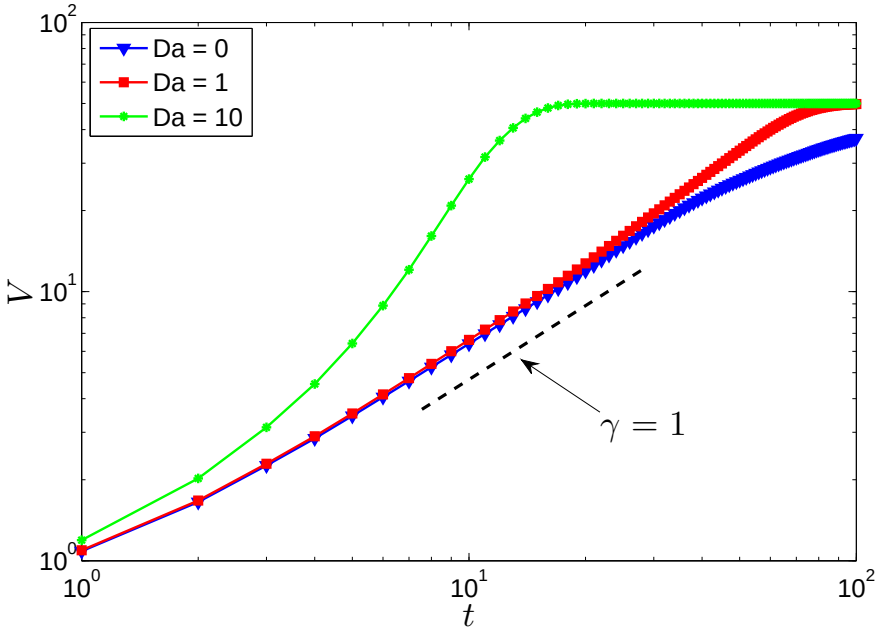

Figure 3.10: Mean-square displacement over time for $Da = 0$ (passive transport), $Da = 1$, and $Da = 10$ for $\Gamma = 10$. The mean-square displacement for $Da = 1$ and $Da = 10$ deviate from normal diffusion.

In Fig. 3.11, the time history of the mean-square displacement for a RD system is given for Damköhler numbers $Da = 0$, $Da = 1/2$, and $Da = 1$ in the $\Gamma = 40$ domain. In the absence of the fluid advection, the mean-square displacement scales with time by $\gamma = 2$. Also plotted in Fig. 3.11 is the mean-square displacement over time for $Da = 0$ which represents a pure diffusive system with $\gamma = 1$. It is interesting to note that these power law relationships for a RD system are similar to those of a RAD system where the fluid advection is due to a time-independent target pattern flow. For the simulations exhibiting spatiotemporal chaos, classifying the scaling laws will help compare the diffusive nature of the spreading compared to those found in RD systems and RAD systems exhibiting simpler flow fields. Figure 3.12 displays the mean-square displacement over time for the Rayleigh number $\mathcal{R} = 6000$. Superdiffusive behavior is also seen in the reacting flows ($Da > 0$) but at a larger scaling exponent than is seen in the previous cases.

Table 3.1 shows power laws extracted from mean-square displacement for all the simulations

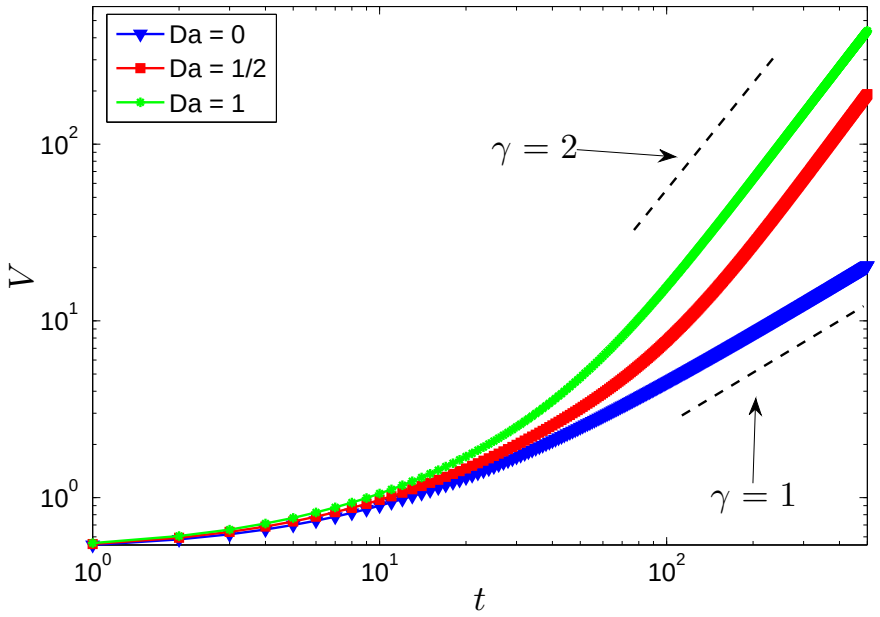

Figure 3.11: The mean-square displacement as a function of time for a RD system for Damköhler numbers $Da = 0$, $Da = 1/2$ and $Da = 1$ in the $\Gamma = 40$ domain. The reactions for $Da = 1/2$ and $Da = 1$ are superdiffusive that scale by an exponent $\gamma = 2$.

in the $\Gamma = 40$ domain. The results show that for active transport for spiral defect chaos describe a superdiffusive process that not only describes anomalous diffusion, but is described by a scaling law γ greater than those found for RD systems in the absence of flow and time-independent target pattern flow. This deviates from the behavior seen in passive transport and suggests that the presence of the spatiotemporally chaotic flows induces strongly anamolous transport for the spreading of an active species.

3.2.4 Front speed enhancement

The speed of a reacting front is an important property related to quantifying active transport in RAD systems. An existing classical theory developed by Kolmogorov [19] describes the front velocity for RD systems to prorogate at a speed of

$$v_f = \sqrt{\frac{2D}{\tau_R}}. \tag{3.9}$$

This theory can be extended to RAD systems that exhibit normal diffusive behavior by using an enhanced molecular diffusivity D^* in place of the D for Eq. (3.9). Unfortunately this may not be applied to the complex flow fields under consideration as the results from the

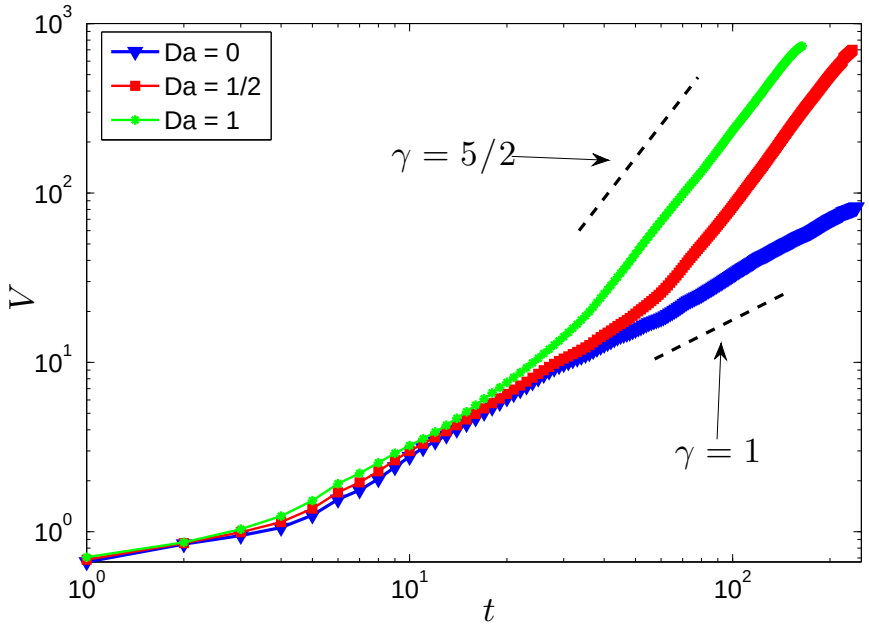

Figure 3.12: Mean-square displacement over time for Damköhler numbers $Da = 0$ (passive transport), $Da = 1/2$, and $Da = 1$ in the $\Gamma = 40$ domain for $\mathcal{R} = 6000$. The reactions for $Da = 1/2$ and $Da = 1$ are superdiffusive that scale by an exponent $\gamma = 5/2$.

previous section indicate superdiffusive behavior. The theory describing anomalous diffusion in RAD systems is still in its infancy. Mancinelli *et al.* [23] advance the theory by deriving linear operators to describe the diffusion and advection effects in reduced RAD systems with relatively slow reactions. These linear operators are functions of the scaling law for the system but also the shape of the probability density function of the diffusive process. Furthermore, this theory is derived for classical flow cases that are unable to be applied in this particular RAD system. However, it is noted that this modified FKPP theory is employed in front prorogation of RAD systems studied in [1] and [2] with simpler, time-independent flow fields. These studies show reaction front speeds dependent on the characteristic fluid velocities for two different reaction regimes. Therefore, the results obtained for front speeds in spiral defect chaos will be compared to those scaling relations.

The front speed in large cylindrical domains is quantified by the time rate of change of the radius of the averaged product spread. This is first done by defining the average growth of the area of products as

$$\frac{dA(t)}{dt} = 2\pi \langle R(t) \rangle_\theta \frac{dR(t)}{dt} \tag{3.10}$$

where $A(t)$ is area of the reacted products, $R(t)$ is the radius of the products spread, and

Da	$\mathcal{R}$	γ
0.5	0 (RD system)	2
	2000	2
	4000	2
	6000	5/2
	20000	2
1	0 (RD system)	2
	2000	2
	4000	5/2
	6000	5/2
	20000	5/2

Table 3.1: Mean-square displacement power laws γ for a variety of flow conditions described by the Rayleigh number $\mathcal{R}$ and the Damköhler number Da. The presence of chaotic Rayleigh-Bénard convection changes the power law scaling from $\gamma = 2$ to $\gamma = 5/2$.

$\langle R(t)\rangle_\theta$ is the azimuthally-averaged radius of the products spread across the domain which is also a function of time and is defined by

$$\langle R(t)\rangle_\theta = \frac{1}{2\pi}\int_0^{2\pi} R(t)\, d\theta. \tag{3.11}$$

The front speed is defined as the quantity, $\frac{dR(t)}{dt}$ and so rearranging Eq. (3.10) the front speed can be defined as

$$\langle v_f(t)\rangle_\theta = \frac{1}{2\pi\,\langle R(t)\rangle_\theta}\frac{dA(t)}{dt}. \tag{3.12}$$

Figure 3.13 shows this azimuthally-averaged velocity as a function of time for active transport for $\Gamma = 40$, $\mathcal{R} = 6000$, $\mathcal{L} = 10^{-1}$ and $Da = 1$. The results show that this front speed experiences an initial transient period in which the speed increases and then oscillates between some maximum value before decreasing again due to the reaction reaching the end of the domain. Equation (3.13) can be used to calculate the front speed averaged over the entire simulation time t_0 which will be used as a comparison with the trends published in the literature. This expression can be obtained by simply taking the time-average of Eq. 3.12 to yield

$$\langle \bar{v}_f\rangle_\theta = \frac{1}{t_0}\int_0^{t_0} \langle v_f(t)\rangle_\theta\, dt. \tag{3.13}$$

Table 3.2 displays the azimuthal- and time-averaged front speed for active transport simula-

tions in the $\Gamma = 10$ domain. The reaction speed increases due to an increase in Damköhler number as what would be expected for the increase in the reaction time scale. The transition to the $\Gamma = 40$ domain allows us to consider a wider number of flow conditions and examine the front speed enhancement.

Da	$\langle \bar{v}_f \rangle_\theta$
1	1.29
10	5.71

Table 3.2: Front speed for $\Gamma = 10$.

Figure 3.14 display the azimuthal- and time-averaged front speed as a function of the characteristic fluid speed U for Damköhler numbers $Da = 1/2$ and $Da = 1$. The plots show a general enhancement in the reaction front speed based on the strength of the flow field. For $Da = 1/2$ the reaction front speed is enhanced by the presence of the flow by a factor $\langle \bar{v}_f \rangle_\theta \propto U^{0.43}$. For $Da = 1$ this enhancement factor becomes $\langle \bar{v}_f \rangle_\theta \propto U^{0.38}$. An interesting feature to point out in these results is the change in front speed during the transition from time-independent to time-dependent spiral defect chaos. The second point in for each set of data in Fig. 3.14 represent the front speed at Rayleigh number $\mathcal{R} = 2000$ which corresponds to a stable state of Rayleigh-Bénard convection that is analogous to a time-independent ring of vortices. The next point in the plot represents the characteristic velocity in Rayleigh number $\mathcal{R} = 4000$ which represents Rayleigh-Bénard convection in the spiral defect chaos state. It is seen that in the $Da = 1/2$ reaction the front speed actually *decreases* in the complex flow field, and then increases as the flow field velocity increases. A similar situation happens in the $Da = 1$ reaction as represented in Fig. 3.14 but while the front speed increases, the rate of increase is much smaller than the other points. This suggests that front inhibition may occur in the transition from stable to chaotic states of Rayleigh-Bénard convection for reactions in advection-dominated transport. More simulations would need to be carried out to investigate further and confirm this behavior.

3.2.5 Transport in terms of local flow field properties

As can be seen in the simulation results that are presented in Fig. 3.1-3.4, one the most interesting features of the chaotic flow fields is their pattern forming qualities. Methods have been developed to quantify the local properties of the flow field by calculating the local wavevectors. Figure 3.15 illustrates how these quantities relate to a flow field pattern.

This section will discuss the attempts to quantify these pattern forming systems in terms of local wavenumbers and derive other important characteristics related to the patterns. Doing so will give qualitative insight into how local convection roll patterns can affect the transport of reactive species. Egolf [11] describes a fast method to determine local properties

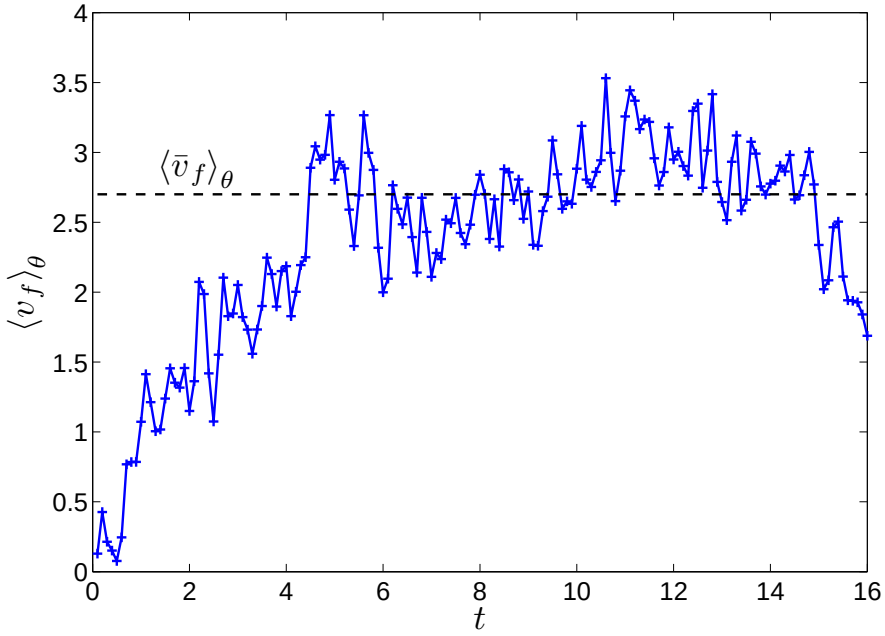

Figure 3.13: Azimuthally-averaged front speed $\langle v_f \rangle_\theta$ as a function of time t for active transport with $\Gamma = 10$, $\mathcal{R} = 6000$, $\mathcal{L} = 10^{-1}$ and $Da = 1$. After an initial transient period, the front speed oscillates between some long-time limit value, denoted by the black dashed line, before decreasing again due to finite-wall effects. The long-time limit value is denoted as the azimuthal- and time-averaged front speed $\langle \bar{v}_f \rangle_\theta$.

in pattern-forming systems which will be employed here. For systems that form a locally striped pattern, each point in a field can be approximated by the function

$$u(\vec{x}) = A(\vec{x}) \cos(\phi(\vec{x})) \tag{3.14}$$

where $u(\vec{x})$ is a field quantity that is a function of cartesian coordinates, $\vec{x}$. The local wavevector is defined as

$$\vec{k}(\hat{x}) \equiv \nabla \phi(\vec{x}). \tag{3.15}$$

The assumption made here is that variations in the value of $A(\vec{x})$ in Eq. (3.14) are small compared to the variations in $\phi(\vec{x})$ and that the local property is sufficiently far from defects and grain boundaries. The components of the local wavenumber in a two-dimensional plane

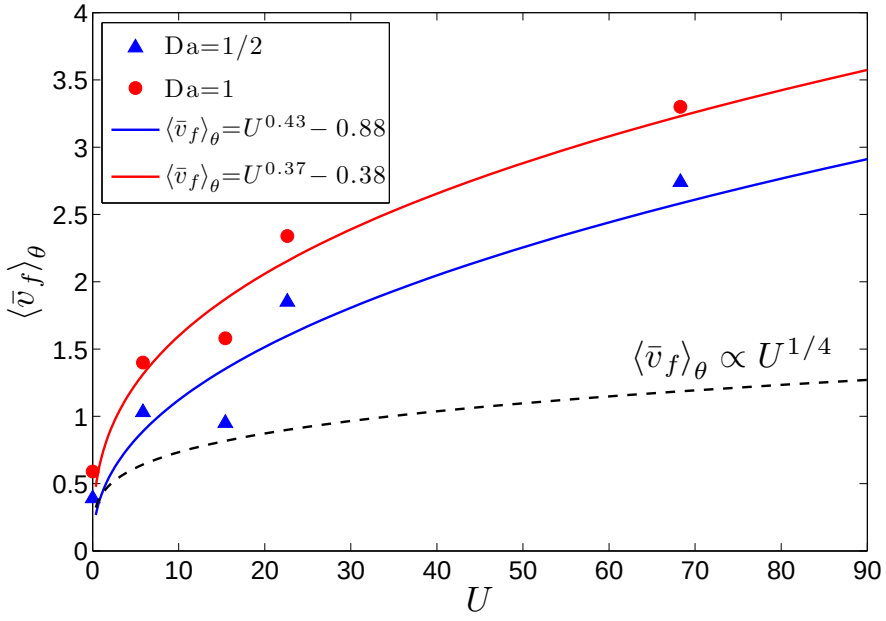

Figure 3.14: The azimuthal- and time-averaged front speed $\langle \bar{v}_f \rangle_\theta$ as a function of the characteristic fluid speed U for reactions at Damköhler numbers $Da = 1/2$ and $Da = 1$. The solid lines represent the fits for both reactions and indicate that for this reaction range, the front speed is enhanced $\langle \bar{v}_f \rangle_\theta \propto U^{2/5}$. The black dashed line represents the upper-bound for a front speed derived for two-dimensional cellular flows found in [1] and [42].

can than be calculated as

$$k_x^2 = -\frac{\partial_x^2 u(\vec{x})}{u(\vec{x})} \tag{3.16}$$

where $k_x \equiv \vec{k} \bullet \hat{x}$ and $\partial_x^2 \equiv \partial^2/\partial_x^2$. The counterpart equation to Eq. (3.21) that can be used to calculate the y-direction wavenumber k_y is

$$k_y^2 = -\frac{\partial_y^2 u(\vec{x})}{u(\vec{x})}. \tag{3.17}$$

This method introduces two problems when analyzing convection rolls in Rayleigh-Bénard convection. First, Eq. (3.21) can be sensitive to small errors introduced through numerical noise. To overcome this problem, Eq. (3.21) and Eq. (3.20) can be replaced with

$$k_x^2 = -\frac{\partial_x^3 u(\vec{x})}{\partial_x u(\vec{x})} \tag{3.18}$$

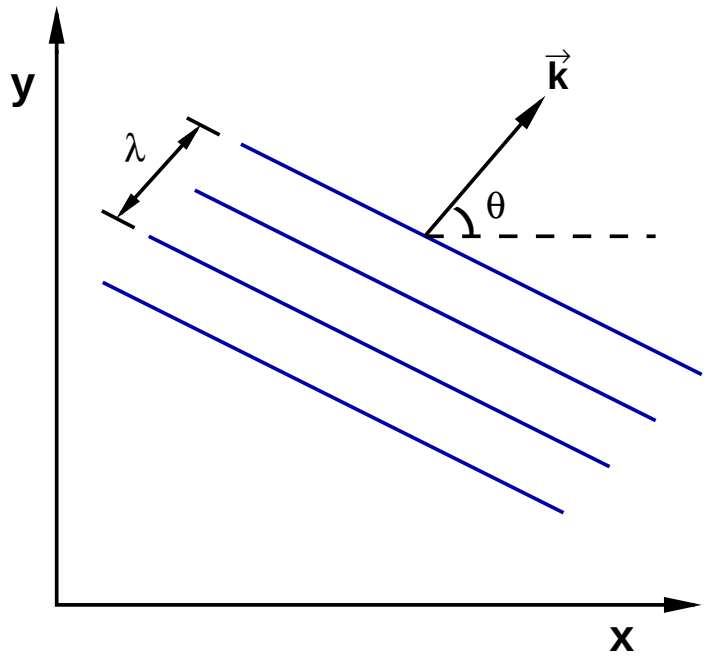

Figure 3.15: Local properties of a flow field where the convection rolls are represented by the blue diagonal lines with a wavelength λ. Perpendicular to the convection rolls is a wavevector defined $\vec{k}$ whose magnitude is the wavenumber k. A roll orientation angle θ is defined as the angle the wavevector forms with the x-axis in cartesian coordinates.

and

$$k_y^2 = -\frac{\partial_y^3 u(\vec{x})}{\partial_y u(\vec{x})} \tag{3.19}$$

respectively. The higher order derivatives in these new expressions can smooth out numerical noise introduced in the system. Second, this method calculates k_x^2 which is a magnitude of a vector and does not conserve any information about the wavevector's orientation. This problem is overcome by keeping the relative sign between the wavevector components in order to preserve directional information. Procedurally, this can be done by first computing the wavevector components using Eq. (3.21) and Eq. (3.20) and then computing the other

components with the equations,

$$k_y = k_x \frac{\partial^2_{xy} u(\vec{x})}{\partial^2_x u(\vec{x})} \tag{3.20}$$

and

$$k_x = k_y \frac{\partial^2_{yx} u(\vec{x})}{\partial^2_y u(\vec{x})}. \tag{3.21}$$

In this procedure k_x will always be a positive value and k_y will contain information about the orientation of the wavedirection. The full procedure is outlined rigorously in [11]. Once the information of the wavevectors are obtained, the local roll orientation angle can be computed by

$$\theta = \arctan\left(\frac{k_y}{k_x}\right). \tag{3.22}$$

The curvature of a roll is defined as the divergence of the wavevector and is calculated using

$$\kappa = \frac{\vec{\nabla} \bullet \hat{k}}{k}. \tag{3.23}$$

Figure 3.16 displays these local properties calculated for a $\Gamma = 40$ and $\mathcal{R} = 6000$ flow field. Figure 3.16(a) displays the deviation from the midplane temperature field. Figure 3.16(b) shows the local wavenumber calculated for this field. The mean wavenumber for this flow field is $k = 2.2$ which falls within the unstable region of the "Busse balloon" [6], as should be expected for this particular Rayleigh-Bénard convection field. Significant deviation from the mean wavenumber are seen in parts of the flow and are shown by the darkened regions. Figure 3.16(c) shows the local roll orientation which using the procedure yields values that range between $-\pi/2 \leq \theta \leq \pi/2$. Lastly, the roll curvature is represented in Fig. 3.16(d), which also shows regions of anomalous values.

From the information of the local properties of the flow field, a horizontal spreading orientation angle can be quantified by

$$\cos(\Phi) = \frac{\nabla c \bullet \vec{k}}{\|\nabla c\| \|\vec{k}\|} \tag{3.24}$$

where Φ is the horizontal spreading orientation, ∇c is the gradient of the concentration field, and $\vec{k}$ is the local wavevector. The horizontal spreading orientation can quantify the spreading of the species relative to the direction of the local wavevector. This gives

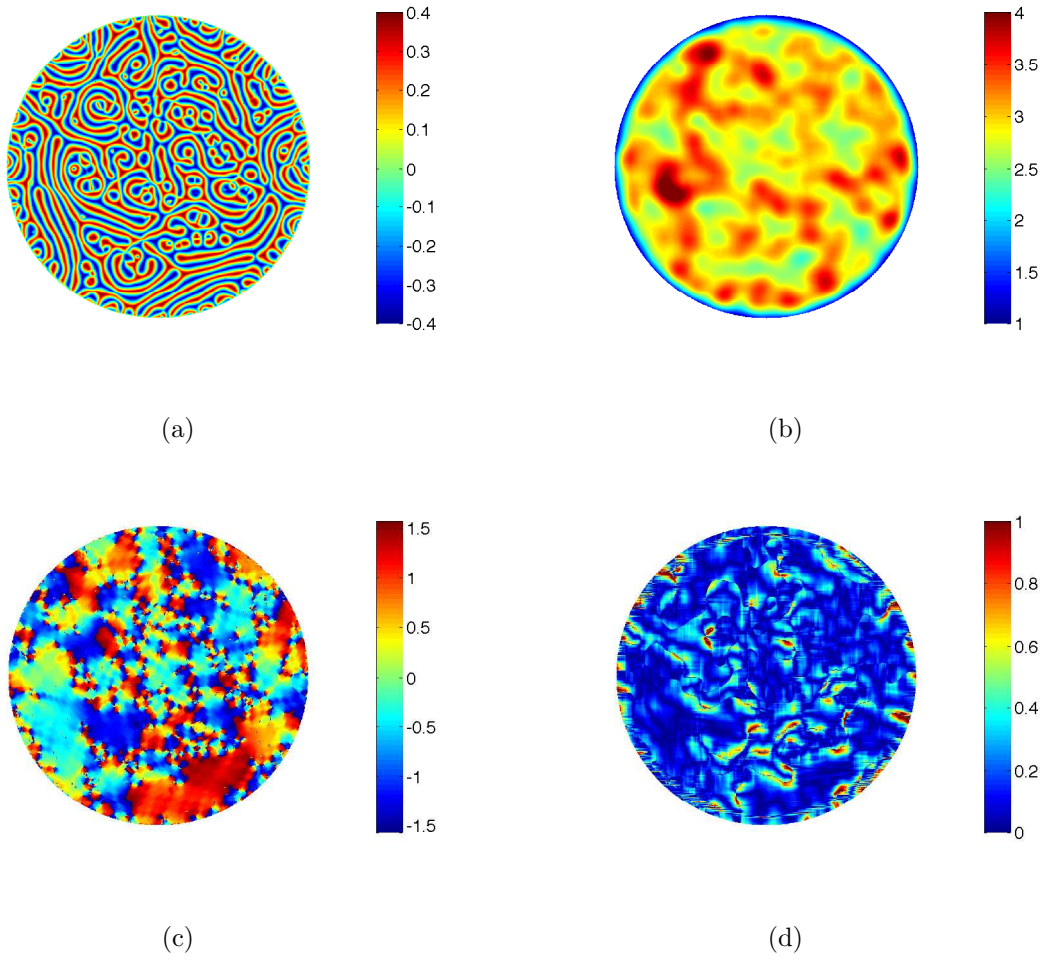

(a) (b)

(c) (d)

Figure 3.16: Local properties of a flow field for $\Gamma = 40$ and $\mathcal{R} = 6000$. Figure 3.16(a) shows the deviation of the temperature field from the midplane values. Figure 3.16(b) is the filtered local wavenumber field. Figure 3.16(c) is the local convection roll orientation. Figure 3.16(d) is the local curvature.

information and insight on how the species spreads across a convection roll. The angle Φ can be calculated at every point in the flow field and quantified statistically. Figure 3.17 shows the probability distribution function of the horizontal spreading orientation at a particular time $t = 5.8$ for active transport for parameters $\Gamma = 40$, $\mathcal{R} = 6000$, and $\mathcal{D}a = 1/2$. This snapshot of the transport shows that the spreading is most likely to occur at $\Phi = \pi/2$, or in a direction perpendicular to a convection roll. The next likely orientation that the spreading will occur is at an angle close to $\Phi = 0$. The spreading is least likely to occur at angles between these two angles. The results shown here are in agreement with those found for passive transport at the same Lewis number $\mathcal{L} = 10^{-1}$ [7]. The mechanisms that explain these trends are attributed to the higher probability that random walks of particles will cross

the separatrix between the convection rolls, as described analytically in [35]. The reason for the larger peak closer to the angle of $\Phi = 0$ must be attributed to the effect of the additional reaction. One speculation for the mechanism at work is the spreading perpendicular to the convection roll might enhance the reaction in *parallel*. More data would need to be collected to test this hypothesis.

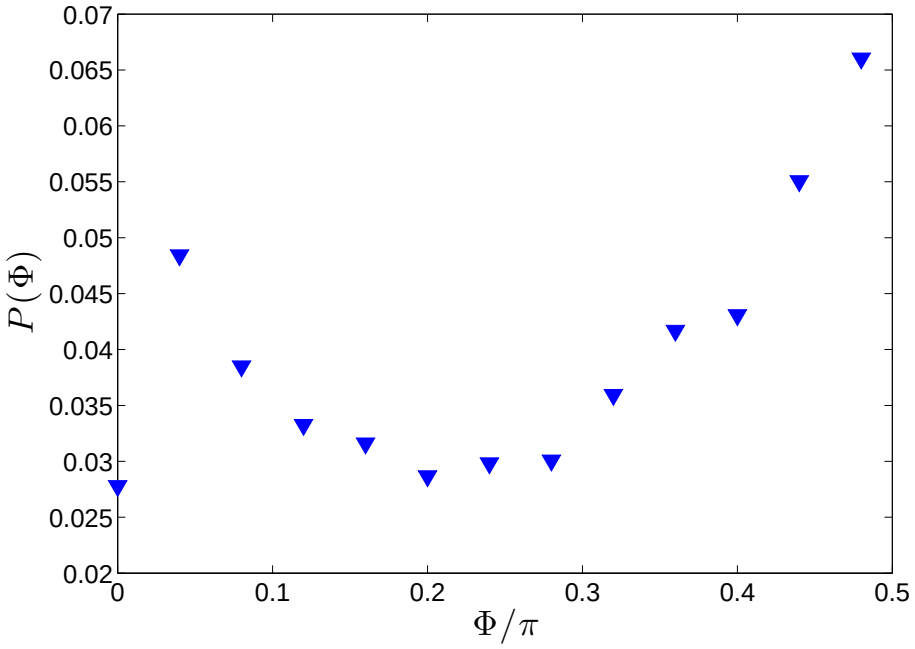

Figure 3.17: Probability distribution function of the horizontal spreading orientation at a time $t = 5.8$ for active transport for parameters $\Gamma = 40$, $\mathcal{R} = 6000$, and $Da = 1/2$. The highest probability of the spreading occurs at an angle $\Phi = \pi/2$

3.2.6 Quantifying front geometry

The emergence of the complex front structure for the active transport simulation results as seen in Fig. 3.4 suggest an enhancement in the front area occurs for reactions in the presence of advection. It has been observed that mixing of active species in RAD systems enhance the the rate of reaction. The physical explanation for this has been attributed to the the increase in the surface area of the front which increases the area available for reactants to change to products [18]. The results obtained in this study suggest that spiral defect chaos also enhances this reaction.

One method that will be used to quantify the front enhancement is to calculate the reaction

area over time for each of the simulations conducted. The reaction area will be defined as

$$A_f = P_f d \tag{3.25}$$

where A_f is the surface area of the front, P_f is the front perimeter and d is the front depth. Since the analysis is reduced to a two-dimensional spread, the depth for the spatially-extended system is $d = 1$. A method is implemented than to track the reaction front for each time and to estimate the front perimeter which in turn gives an estimate for the reaction surface area. Upon observation of the front images in Fig. 3.4, one natural way to estimate the front area is by identifying the the interface between the reactants and products which is roughly quantified by the green boundaries. The criteria used to identify the front is

$$0.45 \leq c\,(x, y, t) \leq 0.55 \tag{3.26}$$

which turns out to be a good estimate of the reaction front. Figure 3.18 is an example of the procedure discussed above applied to a reaction front with a Damköhler number $Da = 1/2$ in a Rayleigh number $\mathcal{R} = 6000$ flow field. From this procedure the reaction front was calculated for each of the active transport simulations. Figures 3.19-3.22 show the front perimeter P_f for reactions at Damköhler numbers $Da = 1/2$ and $Da = 1$ as a function of time for a variety of flow fields. Figure 3.19 shows this trend for a RD system in the absence of any fluid advection. In this case, the front perimeter grows with time according to a unity power law. This power law growth is also observed for a system with advection in the form of a target pattern flow field as indicated in Fig. 3.20. This means that there is no significant enhancement in the surface area of the front with the addition of a time-independent chain of vortices. However, in the transition to a flow field defined by spiral defect chaos, the power law growth increases to slope of 3/2. It is during this transition that the fractal-like structure of the front can be seen.

There have been many methods proposed to quantify fractal-like structures in the field of dynamical systems, including structures that are not self-similar [27] [39]. One simple yet effective method is to calculate the fractal dimension of the geometry using the box-counting method. In this method, a d-dimensional set that represents the reaction front will have an area $N(s)$ that is approximated by the total number of boxes needed with side length s to cover the planer area. Applying this rule yields the relationship

$$N(\epsilon) \propto \frac{1}{s^d}. \tag{3.27}$$

Rearranging Eq. (3.27) and taking the limit as the box side-length approaches zero yields

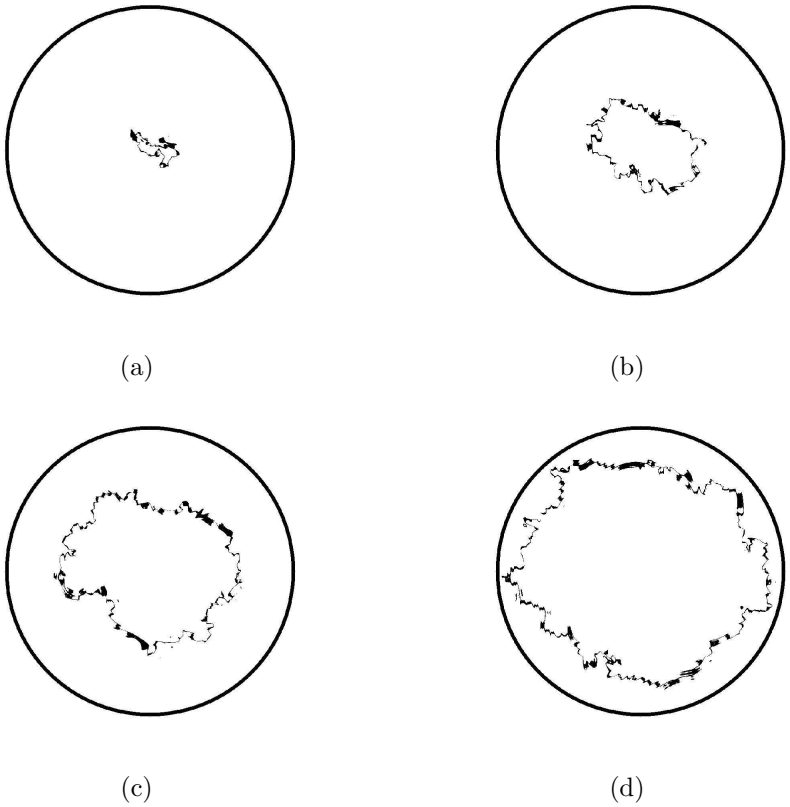

Figure 3.18: Example result of front tracking method for active transport for $\Gamma = 40$, $Da = 1/2$, and $\mathcal{R} = 6000$ for times (a) $t = 5$, (b) $t = 10$, (c) $t = 15$, and (d) $t = 20$.

the definition of the fractal dimension,

$$D_{box} = \lim_{s \to 0} \frac{\ln N(s)}{\ln \frac{1}{s}}. \tag{3.28}$$

Fig. 3.23 shows the fractal dimension calculated for increasingly smaller box side-lengths. The fractal dimension is constant at $D_{box} = 2$ which means that this tool does not capture any fractional dimension. This is likely attributed to finite pixel size of the images processed and therefore other methods must be explored to quantify the front's fractional characteristic.

Another way that was used to quantify the perimeter enhancement of the reaction front is to compare the instantaneous perimeter with a perimeter formed by an azimuthally-averaged radius. Figure 3.24 can aid in visualizing these definitions more clearly. The solid black line in Fig. 3.24 represents the perimeter of the front $P(t)$ at any given time t. This perimeter can be quantified by a perimeter formed by the azimuthally-averaged radius $\langle R(t) \rangle_\theta$ at the same time t. From these definitions an enhancement of the perimeter can be quantified.

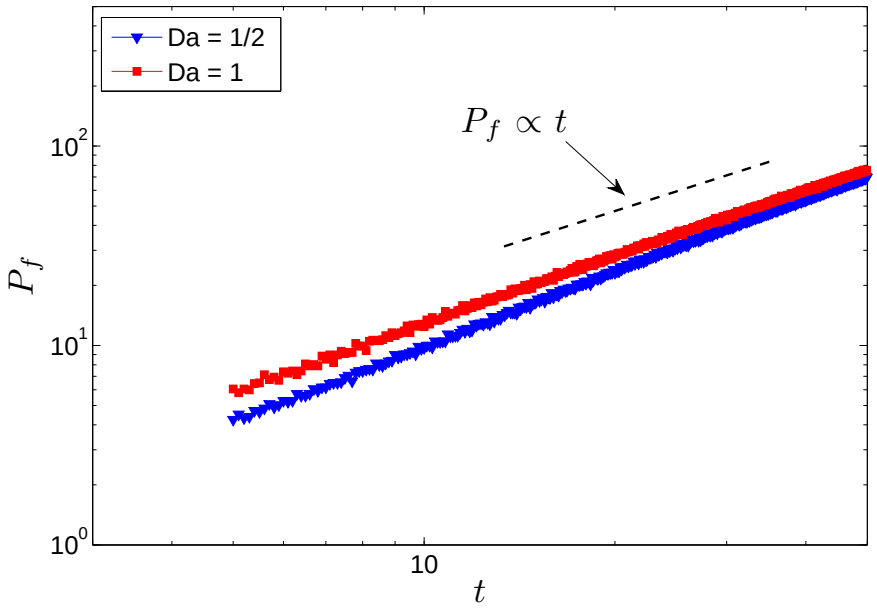

Figure 3.19: Front perimeter P_f over time t for $\Gamma = 40$ in the absence of fluid advection. The front perimeter grows proportionally to time with a power law of unity as indicated by the black dashed line.

A perimeter enhancement ratio is defined as

$$r_p = \frac{P_f(t)}{2\pi \langle R(t) \rangle_\theta}. \tag{3.29}$$

where $\langle R(t) \rangle_\theta$ is the azimuthally-averaged radius of the products spread across the horizontal plane. Figures 3.25-3.27 show r_p as a function of time t for active transport in the absence of fluid flow, for $\mathcal{R} = 2000$, and for $\mathcal{R} = 4000$. The results show a clear enhancement of the front perimeter for a reaction in the presence of spiral defect chaos which was determined to be $r_p = 2.3$ in comparison with identical transport cases within a target pattern flow field ($r_p = 1.8$) and for an RD system ($r_p = 1$). Notice that prominent oscillations in the value of r_p over time that is seen for the transport in the target flow pattern. These can be attributed the mechanism of the front progressing along the time-independent vortex chain across the domain which leads to a front thickening and thinning detected by the method implemented.

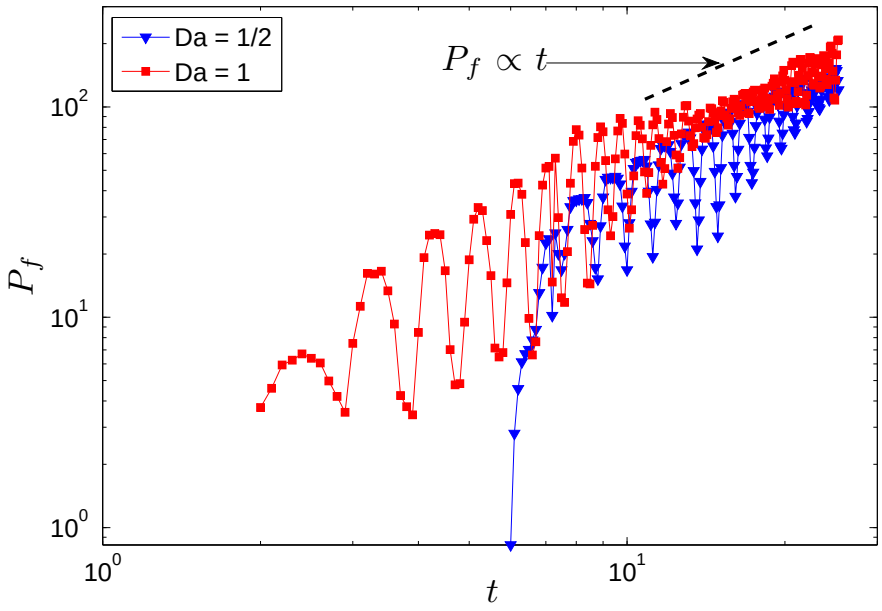

Figure 3.20: Front perimeter P_f over time t for $\Gamma = 40$ and $\mathcal{R} = 2000$. The front perimter grows proportionally to time with a power law of unity as indicated by the black dashed line.

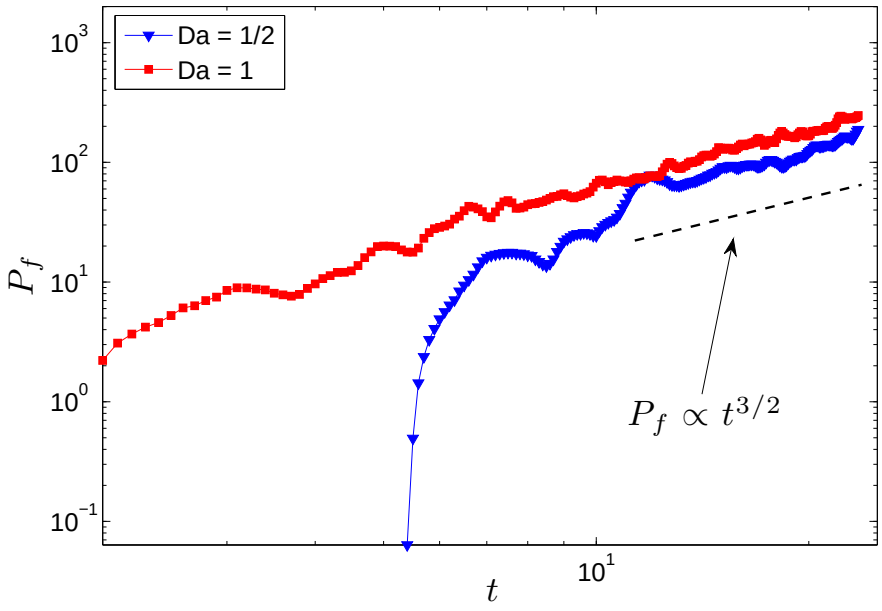

Figure 3.21: Front perimeter P_f over time t for $\Gamma = 40$ and $\mathcal{R} = 4000$. The front perimeter grows proportionally to time with a power law of 3/2 as indicated by the black dashed line.

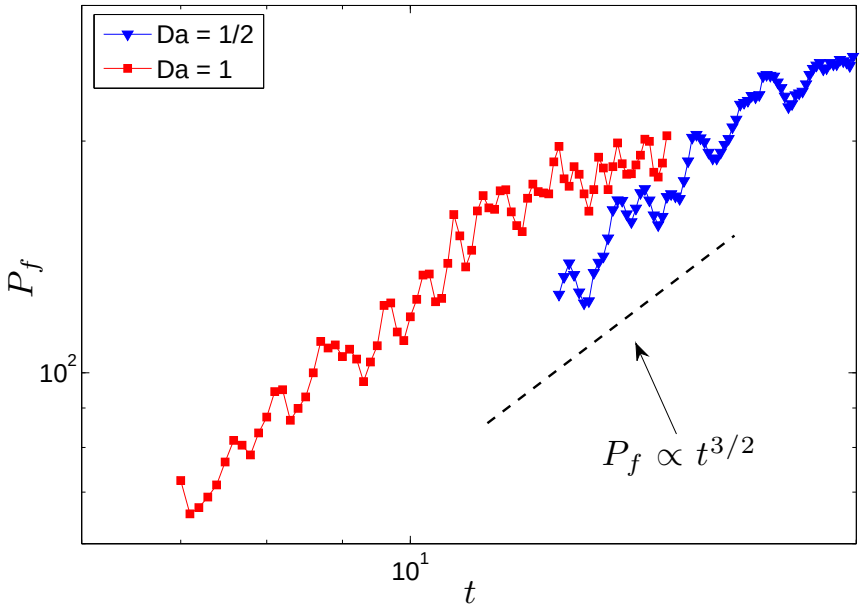

Figure 3.22: Front perimeter P_f over time t for $\Gamma = 40$ and $\mathcal{R} = 6000$. The front perimeter grows proportionally to time with a power law of 3/2 as indicated by the black dashed line.

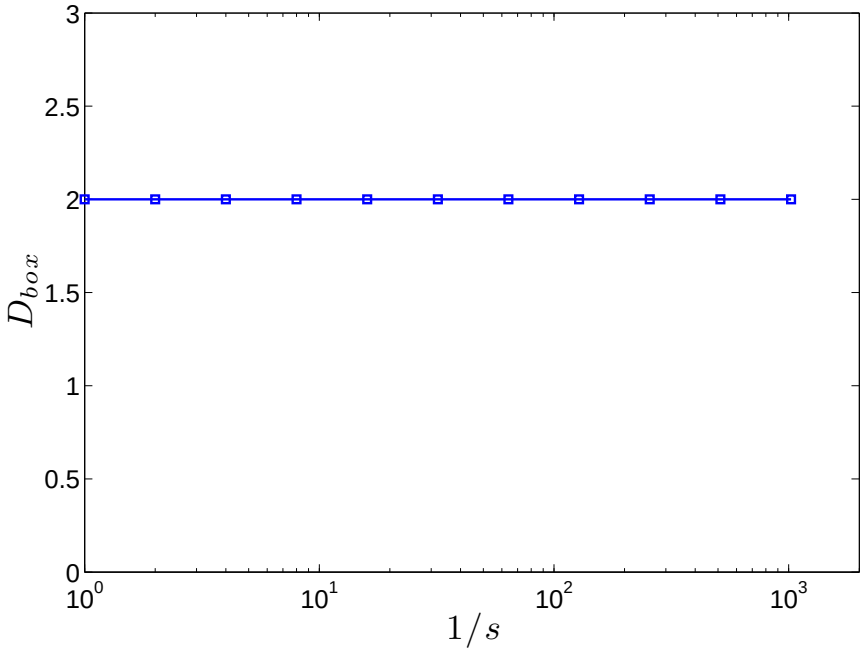

Figure 3.23: Semilog plot of the fractal dimension D_{box} using the box-counting method as a function of the inverse of the box-size $1/s$. As the box size decreases, the dimension remains at a constant value of $D_{box} = 2$.

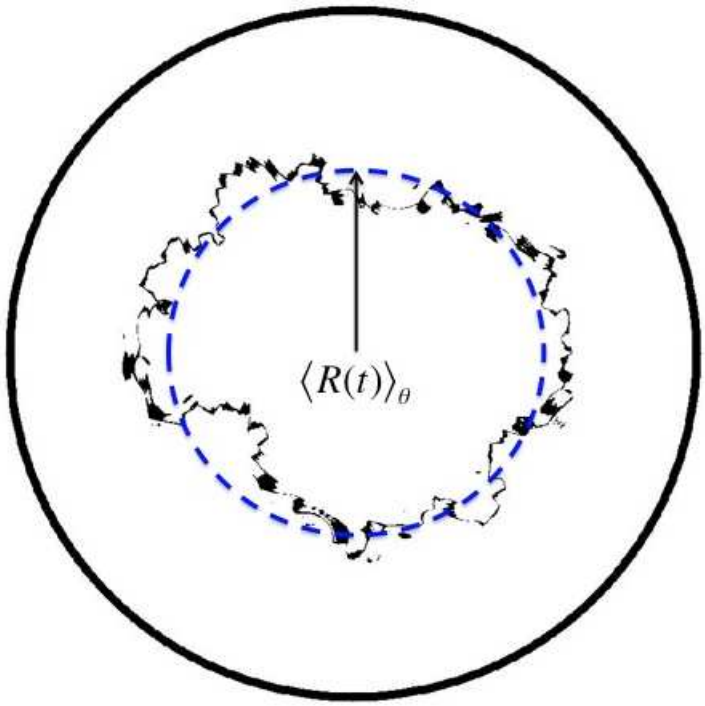

Figure 3.24: Graphic representation of definitions for front dynamics. The solid black line is the perimeter of the front $P_f(t)$ at any given time t. The blue dashed line represents the perimeter formed by the azimuthally-averaged radius $\langle R(t) \rangle_\theta$ at the same time t. The perimeter enhancement ratio r_p is the ratio of these two quantities.

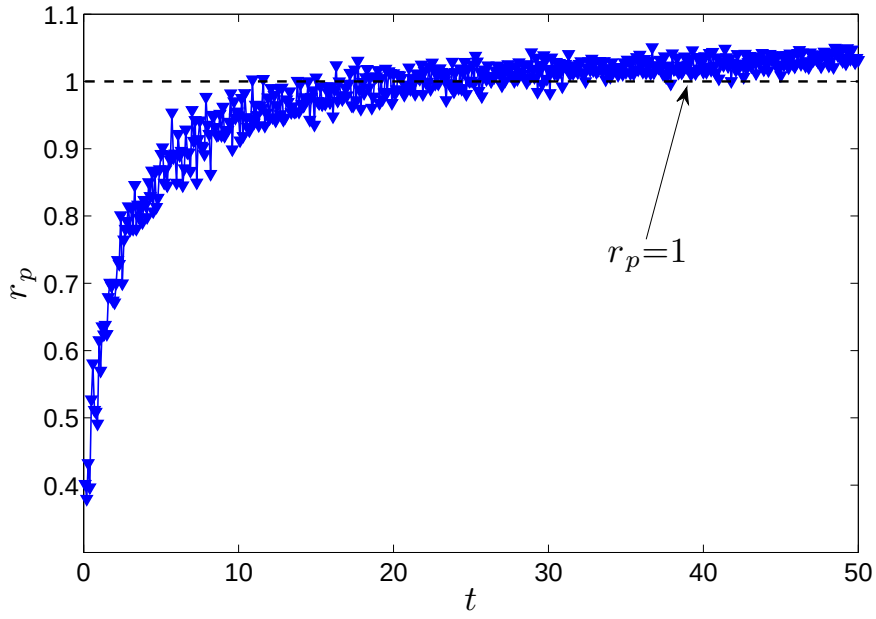

Figure 3.25: The front enhancement ratio r_p as a function of time t for a RD system for $\Gamma = 40$. Ignoring the transient period, the value of r_p becomes one which means that no front enhancement due to the flow field is occurring.

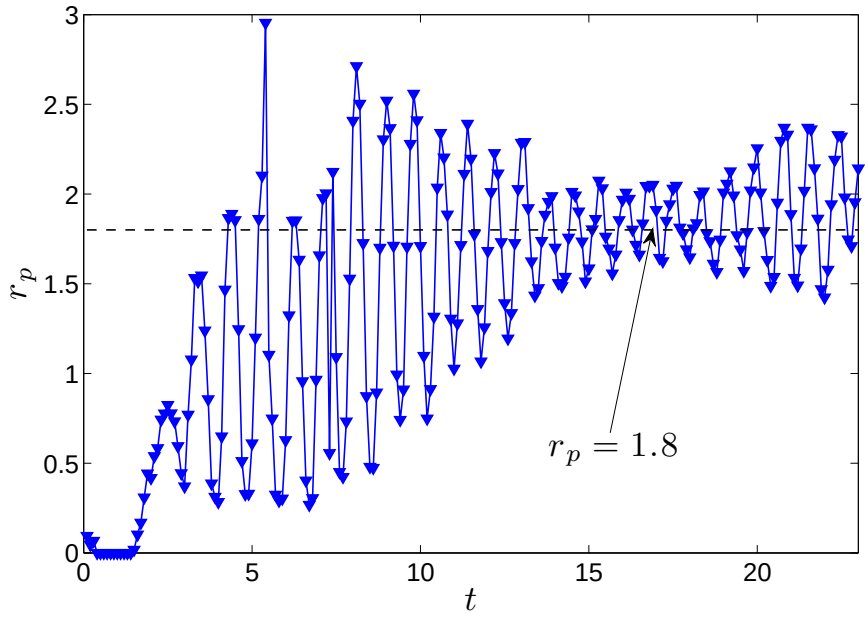

Figure 3.26: The front enhancement ratio r_p as a function of time t for a RAD system for $\Gamma = 40$ and $\mathcal{R} = 2000$. Ignoring the transient period, the value of average front enhancement is $r_p = 1.8$ which means enhancement occurs in the target pattern flow field. The oscillatory response is due to the reaction thickness varying in the presence of the time-independent vortex chain.

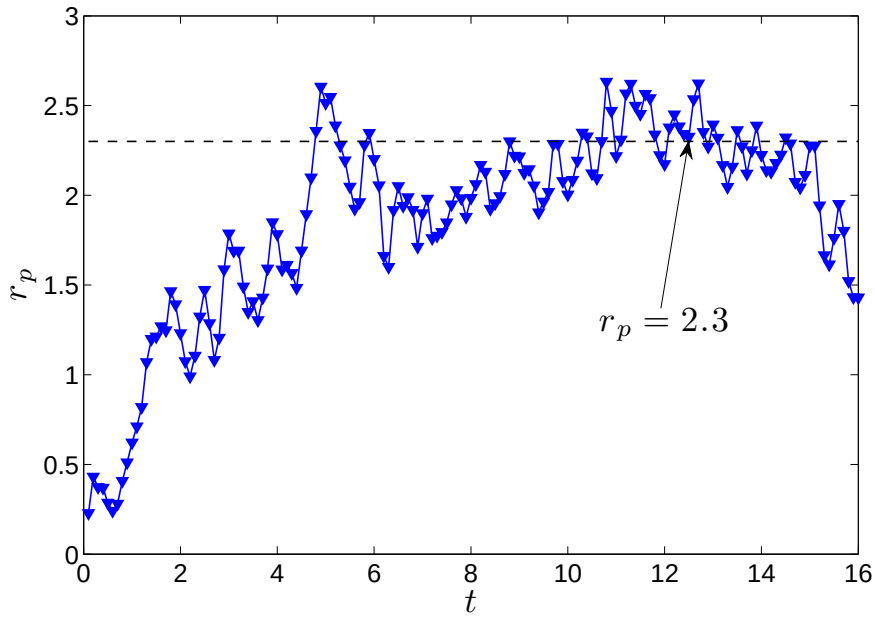

Figure 3.27: The front enhancement ratio r_p as a function of time t for a RAD system for $\Gamma = 40$ and $\mathcal{R} = 6000$. Ignoring the transient period, the value of average front enhancement is $r_p = 2.3$ which means enhancement is greatest in the spiral defect chaos flow field.

Chapter 4

Conclusions

This thesis investigates active transport in a three-dimensional, time-dependent flow field given by chaotic Rayleigh-Bénard convection using high performance numerical simulations. The results show transport enhancement deviates from the enhancement studies in the literature for RAD systems with time-independent and time-periodic flow fields suggesting that the presence of a chaotic flow field further enhances reactions compared to flow fields studied in these previous studies. Three different methods to quantify the transport were studied in this thesis. First, the two-dimensional spreading was quantified statistically by measuring the time history of the mean-square displacement. The spreading of the active species was characterized by anomalous diffusion with scaling exponents between $2.0 \leq \gamma \leq 5/2$. The presence of spiral defect chaos induced strongly anomalous transport. Second, the transport was quantified based on local properties of the convection roll field. These methods showed qualitatively that the roll curvature in the spiral defect chaos flow field affected the reaction spreading. In particular, the horizontal spreading of the species was found to most likely to occur in the direction perpendicular to the convection roll. Third, the geometry of the front was quantified based on a front tracking method and calculation of the fractal dimension. The surface area was found to be enhanced over time due to the presence of the complex field by a factor $t^{3/2}$ when compared to proportionality for the absence of flow and a time-independent target pattern. Finally, the front perimeter for active transport in spiral defect chaos was found to be enhanced over transport in RD and time-independent flows by a perimeter enhancement ratio $r_p = 2.3$.

4.1 Future Work

There are many avenues that can be pursued to expand on the work done in this thesis. The methods to quantify the spreading in this thesis were global methods. Another method that can be pursued is to study the local spreading and stretching of fluid tracers from a

Lagrangian perspective. By doing so, one is able to quantify the local stretching using the spectrum of Lyapunov exponents. Shadden *et al.* [34] provides a comprehensive overview of this procedure that has been well-established for research in dynamical systems and shows its natural extension to fluid systems, where transport of passive tracers are studied using quantities like Finite Time Lyapunov Exponents (FTLE). Taking a Lagrangian approach to the research presented in this thesis would take steps towards connecting the insights gained here to other modern approaches to RAD systems – in particular, those pertaining to BIMs.

Bibliography

[1] M. Abel, A. Celani, D. Vergni, and A. Vulpiani. Front propagation in laminar flows. *Physical Review E*, 64(4):046307, 2001.

[2] M. Abel, D. Cencini, D. Vergni, and A. Vulpiani. Front speed enhancement in cellular flows. *Chaos: An Interdisciplinary Journal of Nonlinear Science*, 12:481–488, 2002.

[3] H. Aref. Stirring by chaotic advection. *Journal of Fluid Mechanics*, 143(1):121, 1984.

[4] D. Bargteil and T. H. Solomon. Barriers to front propagation in ordered and disordered vortex flows. *Chaos: An Interdisciplinary Journal of Nonlinear Science*, 22(3):037103037103, 2012.

[5] D. Barkley. A model for fast computer simulation of waves in excitable media. *Physica D: Nonlinear Phenomena*, 49(1):6170, 1991.

[6] E. Bodenschatz, W. Pesch, and G. Ahlers. Recent developments in Rayleigh-Bénard convection. *Annual Review of Fluid Mechanics*, 32(1):709–778, 2000.

[7] K.-H. Chiam, M. C. Cross, H. S. Greenside, and P. F. Fischer. Enhanced tracer transport by the spiral defect chaos state of a convecting fluid. *Physical Review E*, 71(3):036205, 2005.

[8] M. C. Cross and H. S. Greenside. *Pattern formation and dynamics in nonequilibrium systems*. Cambridge University Press Cambridge, 2009.

[9] M. O. Deville, P. F. Fischer, and E. H. Mund. *High-order methods for incompressible fluid flow*, volume 9. Cambridge University Press, 2002.

[10] D. A. Egolf and H. S. Greenside. Relation between fractal dimension and spatial correlation length for extensive chaos. *Nature*, 369(6476):129131, 1994.

[11] D. A. Egolf, I. V. Melnikov, and E. Bodenschatz. Importance of local pattern properties in spiral defect chaos. *Physical Review Letters*, 80:3228–3231, Apr 1998.

[12] P. Falkowski. Ocean science: The power of plankton. *Nature*, 483(7387):S17S20, 2012.

[13] P. F. Fischer. An overlapping schwarz method for spectral element solution of the incompressible Navier-Stokes equations. *Journal of Computational Physics*, 133(1):84101, 1997.

[14] L. Glass. Synchronization and rhythmic processes in physiology. *Nature*, 410(6825):277284, 2001.

[15] A. L. Hodgkin and A. F. Huxley. A quantitative description of membrane current and its application to conduction and excitation in nerve. *The Journal of Physiology*, 117(4):500, 1952.

[16] A. Karimi and M. R. Paul. Quantifying spatiotemporal chaos in Rayleigh-Bénard convection. *Physical Review E*, 85(4):046201, 2012.

[17] B. Kirby. *Micro-and nanoscale fluid mechanics*. Cambridge University Press, 2010.

[18] A. Kiselev and L. Ryzhik. Enhancement of the traveling front speeds in reaction-diffusion equations with advection. In *Annales de l'Institut Henri Poincare (C) Non Linear Analysis*, volume 18, pages 309–358. Elsevier, 2001.

[19] A. N. Kolmogorov, I. G. Petrovskii, and N. S. Piskunov. A study of the equation of diffusion with increase in the quantity of matter, and its application to a biological problem. *Bjul. Moskovskogo Gos. Univ*, 1(7):126, 1937.

[20] A. Libchaber, C. Laroche, and S. Fauve. Period doubling cascade in mercury, a quantitative measurement. *Journal de Physique Lettres*, 43(7):211–216, 1982.

[21] E. N. Lorenz. Deterministic nonperiodic flow. *Journal of the Atmospheric Sciences*, 20(2):130141, 1963.

[22] J. R. Mahoney, D. Bargteil, M. Kingsbury, K. A. Mitchell, and T. H. Solomon. Invariant barriers to reactive front propagation in fluid flows. *EPL (Europhysics Letters)*, 98(4):44005, 2012.

[23] R. Mancinelli, D. Vergni, and A. Vulpiani. Front propagation in reactive systems with anomalous diffusion. *Physica D: Nonlinear Phenomena*, 185(3):175–195, 2003.

[24] R. M. May. Simple mathematical models with very complicated dynamics. *Nature*, 261(5560):459–467, 1976.

[25] K. A. Mitchell and J. R. Mahoney. Invariant manifolds and the geometry of front propagation in fluid flows. *Chaos: An Interdisciplinary Journal of Nonlinear Science*, 22(3):037104037104, 2012.

[26] C. R. Nugent, W. M. Quarles, and T. H. Solomon. Experimental studies of pattern formation in a reaction-advection-diffusion system. *Physical Review Letters*, 93(21):218301, 2004.

[27] E. Ott. *Chaos in dynamical systems*. Cambridge University Press, 2002.

[28] M. S. Paoletti, C. R. Nugent, and T. H. Solomon. Synchronization of oscillating reactions in an extended fluid system. *Physical Review Letters*, 96(12):124101, 2006.

[29] M. S. Paoletti and T. H. Solomon. Experimental studies of front propagation and mode-locking in an advection-reaction-diffusion system. *EPL (Europhysics Letters)*, 69(5):819, 2005.

[30] T. Peacock and G. Haller. Lagrangian coherent structures: The hidden skeleton of fluid flows. *Physics Today*, 66(2):4147, 2013.

[31] M. N. Rosenbluth, H. L. Berk, I. Doxas, and W. Horton. Effective diffusion in laminar convective flows. *Physics of Fluids*, 30:2636, 1987.

[32] H. G. Schuster and R. Grigoriev. *Transport and Mixing in Laminar Flows: From Microfluidics to Oceanic Currents*. Wiley. com, 2012.

[33] M. E. Schwartz and T. H. Solomon. Chemical reaction fronts in ordered and disordered cellular flows with opposing winds. *Physical Review Letters*, 100(2):028302, 2008.

[34] S. C. Shadden, F. Lekien, and J. E Marsden. Definition and properties of Lagrangian coherent structures from finite-time Lyapunov exponents in two-dimensional aperiodic flows. *Physica D: Nonlinear Phenomena*, 212(3):271–304, 2005.

[35] B. I. Shraiman. Diffusive transport in a Rayleigh-Bénard convection cell. *Physical Review A*, 36(1):261, 1987.

[36] R. H. Simoyi, A. Wolf, and H. L Swinney. One-dimensional dynamics in a multicomponent chemical reaction. *Physical Review Letters*, 49(4):245, 1982.

[37] T. H. Solomon and J. P. Gollub. Chaotic particle transport in time-dependent Rayleigh-Bénard convection. *Physical Review A*, 38(12):6280, 1988.

[38] T. H. Solomon and J. P. Gollub. Passive transport in steady Rayleigh-Bénard convection. *Physics of Fluids*, 31:1372, 1988.

[39] S. Strogatz. Nonlinear dynamics and chaos: with applications to physics, biology, chemistry and engineering. 2001.

[40] H. M. Tufo and P. F. Fischer. Terascale spectral element algorithms and implementations. In *Proceedings of the 1999 ACM/IEEE conference on Supercomputing (CDROM)*, page 68. ACM, 1999.

[41] A. M. Turing. The chemical basis of morphogenesis. *Bulletin of Mathematical Biology*, 52(1):153197, 1990.

[42] N. Vladimirova, P. Constantin, A. Kiselev, O. Ruchayskiy, and L. Ryzhik. Flame enhancement and quenching in fluid flows. *Combustion Theory Modelling*, 7(3):487508, 2003.

[43] A. Wolf, J. B. Swift, H. L. Swinney, and J. A. Vastano. Determining Lyapunov exponents from a time series. *Physica D: Nonlinear Phenomena*, 16(3):285317, 1985.